


## AUTHOR QUERY FORM

	<p>Journal: Phys. Fluids</p> <p>Article Number: POF24-AR-15588</p>	<p>Please provide your responses and any corrections by annotating this PDF and uploading it to AIP's eProof website as detailed in the Welcome email.</p>
---	--	--

Dear Author,

Below are the queries associated with your article; please answer all of these queries before sending the proof back to AIP.

**Article checklist:** In order to ensure greater accuracy, please check the following and make all necessary corrections before returning your proof.

1. Is the title of your article accurate and spelled correctly?
2. Please check affiliations including spelling, completeness, and correct linking to authors.
3. Did you remember to include acknowledgment of funding, if required, and is it accurate?

Location in article	Query / Remark: click on the Q link to navigate to the appropriate spot in the proof. There, insert your comments as a PDF annotation.
AQ1	Please check that the author names are in the proper order and spelled correctly. Also, please ensure that each author's given and surnames have been correctly identified (given names are highlighted in red and surnames appear in blue).
AQ2	<p>We were unable to locate a digital object identifier (doi) for Ref(s). Tan and Zhang (2003). Please verify and correct author names and journal details (journal title, volume number, page number, and year) as needed and provide the doi. If a doi is not available, no other information is needed from you. For additional information on doi's, please select this link: <a href="http://www.doi.org/">http://www.doi.org/</a>.</p> <p>Please confirm ORCID's are accurate. If you wish to add an ORCID for any author that does not have one, you may do so now. For more information on ORCID, see <a href="https://orcid.org/">https://orcid.org/</a>.</p> <p>Jordi Pallares - 0000-0003-0305-2714</p> <p>Alexandre Fabregat - 0000-0002-6032-2605</p> <p>Akim Lavrinenko - 0000-0002-0344-4622</p> <p>Nelson Marques - 0000-0002-2265-5548</p> <p>Bruno Santos - 0009-0002-0084-2884</p> <p>Gabriele Mosca - 0009-0006-8168-5073</p> <p>Pedro Obando Vega-</p> <p>Jure Ravnik - 0000-0002-7993-6738</p> <p>Nejc Vovk-</p> <p>Bruño Fraga - 0000-0003-3444-7559</p> <p>Aleksandra Monka - 0009-0004-0553-6311</p> <p>Manuel Martínez - 0000-0003-3910-5224</p> <p>Naomi Mestre-Curto - 0009-0003-7676-6432</p>

Francisco Jose de Souza - 0000-0002-1993-7480  
Douglas Fontes - 0000-0001-8019-8114  
Natalie Jüngling - 0000-0002-3517-5068  
Jennifer Niessner - 0000-0002-4141-2541  
Robert Castilla - 0000-0002-3848-2004  
Mercè Garcia Vilchez - 0009-0008-0472-4221  
David F. Fletcher - 0000-0003-2221-4192  
Kiao Inthavong - 0000-0003-0476-0237  
Matjaž Hriberšek-  
Paul Steinmann - 0000-0003-1490-947X  
Jana Wedel-  
Florent Duchaine-  
Shriram Sankurantripati - 0009-0001-6552-285X  
Leo Amari - 0009-0003-7725-2513  
Gábor Janiga - 0000-0002-4560-9640  
Cristian Marchioli-  
Salvatore Cito - 0000-0001-7626-3374

Please check and confirm the Funder(s) and Grant Reference Number(s) provided with your submission:

UK National Supercomputing Service, Award/Contract Number

National Computational Infrastructure, Award/Contract Number

Très Grand Centre de Calcul du CEA, Award/Contract Number A0162A06074

MWK Baden-Württemberg, Award/Contract Number 32-7545.20/4/59

Ministerio de Ciencia e Innovación, Award/Contract Number PID2020-113303GB-C21

Ministerio de Ciencia e Innovación, Award/Contract Number PID2023-146648NB-C21

Generalitat de Catalunya, Award/Contract Number 2021SGR00732

Please add any additional funding sources not stated above:

Thank you for your assistance.

# Computational fluid dynamics challenge on indoor dispersion of pathogen-laden aerosols

Cite as: Phys. Fluids **37**, 000000 (2025); doi: 10.1063/5.0252665

Submitted: 11 December 2024 · Accepted: 30 January 2025 ·

Published Online: 0 Month 0000



AQ1

Jordi Pallares,<sup>1</sup> Alexandre Fabregat,<sup>1,a)</sup> Akim Lavrinenko,<sup>1</sup> Nelson Marques,<sup>2,3</sup> Bruno Santos,<sup>2</sup> Gabriele Mosca,<sup>4</sup> Pedro Obando Vega,<sup>4</sup> Jure Ravnik,<sup>5</sup> Nejc Vovk,<sup>5</sup> Bruño Fraga,<sup>6</sup> Aleksandra Monka,<sup>6</sup> Manuel Martínez,<sup>7</sup> Naomi Mestre-Curto,<sup>7</sup> Francisco Jose de Souza,<sup>8</sup> Douglas Fontes,<sup>9</sup> Natalie Jüngling,<sup>10</sup> Jennifer Niessner,<sup>10</sup> Robert Castilla,<sup>11</sup> Mercè Garcia Vilchez,<sup>11</sup> David F. Fletcher,<sup>12</sup> Kiao Inthavong,<sup>13</sup> Matjaž Hriberšek,<sup>5</sup> Paul Steinmann,<sup>14</sup> Jana Wedel,<sup>14</sup> Florent Duchaine,<sup>15</sup> Shriram Sankuranthipati,<sup>15</sup> Leo Amari,<sup>16</sup> Gábor Janiga,<sup>16</sup> Cristian Marchioli,<sup>17</sup> and Salvatore Cito<sup>1</sup>

## AFFILIATIONS

<sup>1</sup>Departament d'Enginyeria Mecànica, Universitat Rovira i Virgili, Av. Països Catalans, 26, 43007-Tarragona, Spain

<sup>2</sup>FS Dynamics Portugal, Rua Fonte dos Corvos 29, Casais da Serra, 2665-305 Milharado, Portugal

<sup>3</sup>Department of Mechanical Engineering, ISEL, Rua Conselheiro Emídio Navarro 35, 1950-062 Lisboa, Portugal

<sup>4</sup>Buildwind, Rue Bara 175, 1070 Brussels, Belgium

<sup>5</sup>Faculty of Mechanical Engineering, University of Maribor, Smetanova 17, SI-2000, Maribor, Slovenia

<sup>6</sup>Department of Civil Engineering, University of Birmingham, Edgbaston, Birmingham, B15 2TT, United Kingdom

<sup>7</sup>Eurecat, Centre Tecnològic de Catalunya, Water, Air and Soil Unit, C. Marcel·lí Domingo 2, 43007-Tarragona, Spain

<sup>8</sup>School of Mechanical Engineering, Federal University of Uberlândia, Uberlândia 38400-902, Brazil

<sup>9</sup>Engineering Program, Westmont College, 955 La Paz Rd., Santa Barbara, California 93108, United States of America

<sup>10</sup>Institute for Flow in Additively Manufactured Porous Media, Heilbronn University of Applied Sciences, Max-Planck-Str. 39, 74081-Heilbronn, Germany

<sup>11</sup>CATMech- Fluid Mechanics Department, Universitat Politècnica de Catalunya, Carrer Colom, 1-11, 08222-Terrassa, Spain

<sup>12</sup>School of Chemical and Biomolecular Engineering, The University of Sydney, Sydney, Australia

<sup>13</sup>Mechanical & Automotive Engineering, School of Engineering, RMIT University, Bundoora, Victoria 3083, Australia

<sup>14</sup>Institute of Applied Mechanics, University of Erlangen Nuremberg, Erlangen, Germany

<sup>15</sup>CERFACS, 42 Avenue Gaspard Coriolis, 31 057 Toulouse, Cedex 01, France

<sup>16</sup>Laboratory of Fluid Dynamics and Technical Flows, Otto von Guericke University of Magdeburg, Germany

<sup>17</sup>Department of Engineering and Architecture, University of Udine, Via delle Scienze 208, 33100 Udine, Italy

<sup>a)</sup> Author to whom correspondence should be addressed: alexandre.fabregat@urv.cat

## ABSTRACT

This paper presents and discusses the results of the “2024 International Computational Fluid Dynamics Challenge on the long-range indoor dispersion of pathogen-laden aerosols” aimed at assessing the ability of different computational codes and turbulence models to reproduce the dispersion of particles produced by a turbulent natural convection flow enclosed in a room sized cubical cavity. A total of 12 research groups from ten different countries have conducted 15 simulations of the same flow configuration by solving the Reynolds averaged Navier–Stokes (RANS) equations, the unsteady Reynolds averaged Navier–Stokes (URANS) equations or using scale adaptive simulations (SAS), large-eddy simulations (LES), or hybrid (URANS-LES) techniques. Results for the velocity field and the particle dispersion provided by the different simulations are compared extensively, including the reference results provided by a direct numerical simulation (DNS). In general, LES and hybrid methods reproduce the time-averaged flow field correctly, the spatial distribution of the turbulence kinetic energy, and the particle dispersion. The performance of SAS is similar to that of LES and hybrid methods while the predictions of the RANS and URANS simulations exhibit larger deviations with respect to DNS. In general, the particle dispersion is better reproduced by simulations that capture correctly the spatial distribution of the turbulence kinetic energy.

Published under an exclusive license by AIP Publishing. <https://doi.org/10.1063/5.0252665>

## 46 I. INTRODUCTION

47 Good indoor air quality is important for human health. Long-  
 48 term exposure to air pollution can cause several health problems  
 49 (Maroni *et al.*, 1995). The list of potential contaminants is long and  
 50 includes chemicals, smoke, biological pollutants, and particulate matter  
 51 (PM), among others (Jones, 1999; Seguel *et al.*, 2017; WHO, 2010).  
 52 Indoor PM encompasses solid and/or liquid particles suspended in air,  
 53 and concerns are focused on particles that are 10 micrometers in size  
 54 or smaller (PM<sub>10</sub>) because these particles are inhalable and can affect  
 55 the lungs and the heart (Riley *et al.* 2002; Tan and Zhang, 2003).  
 56 Indoor PM is generated, among other sources, by cooking, cleaning,  
 57 and combustion activities, printers, animals, mold, as well as humans,  
 58 when breathing, speaking, singing, sneezing, or coughing (Li *et al.*,  
 59 2017). The pathogen-laden aerosols generated during these respiratory  
 60 events by an infected person are known to be the route of transmission  
 61 of some respiratory diseases (Bourouiba, 2021).

62 Computational fluid dynamics (CFD) has been essential in ana-  
 63 lyzing and predicting indoor airflows in the last few decades (Li and  
 64 Nielsen, 2011). Most of the CFD based studies have been oriented  
 65 toward understanding and improving ventilation strategies (Cuce *et al.*  
 66 2019, Yerragolam *et al.*, 2024), determining the exposure to pollutants  
 67 (Shen *et al.* 2013, Choi *et al.*, 2019; Concilio *et al.*, 2024), analysis of  
 68 the dispersion and deposition of PM (Xu and Wang, 2017), or estab-  
 69 lishing the risk of infection by pathogen laden aerosols (Ai and  
 70 Melikov, 2018, Sheikhejad *et al.*, 2022; Shim *et al.*, 2023). Simulations  
 71 of indoor ventilation have been performed mostly using the numerical  
 72 solutions of the Reynolds averaged Navier–Stokes (RANS) equations  
 73 and, to a lesser extent, with large-eddy simulations (LES) techniques  
 74 (Caciolo *et al.* 2012). The relatively high Reynolds number, with length  
 75 scales on the order of several meters and velocities of several tens of  
 76 meters per second, makes the current use of direct numerical simu-  
 77 lations (DNS) almost unfeasible nowadays due to the extremely high  
 78 computational cost (Yerragolam *et al.*, 2024; Yang *et al.*, 2022). In  
 79 addition, the typical forced ventilation strategies encountered in real  
 80 scenarios, which include free and/or wall jets interacting with thermal  
 81 stratification and buoyancy effects, produce very different turbulence  
 82 levels. In turn, this results in different turbulence lengths and time  
 83 scales, in different locations of the room, which is usually characterized  
 84 by complex geometry (furniture, persons, etc.) and complex boundary  
 85 conditions (windows, heaters, fans, etc.). The assessment of the perfor-  
 86 mance of RANS and LES approaches has been analyzed by comparing  
 87 the numerical predictions with experiments (Bournet and Boulard  
 88 2010; Caciolo *et al.* 2012; Villafuela *et al.*, 2013; Gilani *et al.* 2016; van  
 89 Hooff *et al.*, 2017). This comparison is often influenced by the finite  
 90 number of measurements that can be obtained experimentally and by  
 91 the uncertainty of the measurements themselves and of the boundary  
 92 conditions.

93 This paper presents and discusses extensive comparisons of  
 94 numerical simulations of the flow and particle dispersion in a proto-  
 95 typical room. These simulations have been performed by different  
 96 research groups in the framework of an international CFD challenge.  
 97 The goal of this collaborative study is to assess the performance of  
 98 computationally efficient turbulence modeling techniques, specifically  
 99 those based on LES, SAS, and RANS simulations within a well-defined  
 100 and controlled flow configuration. We have selected a simplified flow  
 101 setup that permits the use of DNS, enabling us to obtain comprehen-  
 102 sive reference data on turbulent flow and particle dispersion. These

data serve as a benchmark for comparison with the LES, SAS, and 103  
 RANS simulation results. We have considered the enclosed turbulent 104  
 natural convection flow generated by imposing a temperature differ- 105  
 ence on two pairs of horizontal and vertical walls of a room-size cubi- 106  
 cal cavity. 107

DNS of turbulent natural convection flows in cubical enclosures 108  
 have been performed for different combinations of heated and cooled 109  
 walls. In particular, turbulent Rayleigh–Bénard convection (Demou 110  
 and Grigoriadis, 2019, Vasiliev *et al.*, 2019, Delort-Laval *et al.*, 2022) 111  
 and the turbulent free convection generated in the side-heated cubical 112  
 enclosure (Tric *et al.*, 2000; Salat *et al.*, 2004; Kalilainen *et al.*, 2016; 113  
 Dehbi *et al.*, 2017; Wang *et al.*, 2017) have been extensively investi- 114  
 gated. Other combinations of heated and cooled walls include the 115  
 mixed cavity free convection with simultaneously imposed vertical and 116  
 horizontal temperature gradients (Hanjalić and Vasić, 1993; 117  
 Teimurazov *et al.* 2021). In this particular flow configuration, the ori- 118  
 entation and the direction of fluid rotation within the large-scale cir- 119  
 culation are fixed and determined by the thermally active vertical walls. 120  
 This is in contrast to the classical Rayleigh–Bénard problem in a cubic 121  
 cavity, heated from below and cooled from above, with adiabatic verti- 122  
 cal walls. In this scenario, the large-scale circulation changes the orien- 123  
 tation with a relatively low frequency (Soucassee *et al.*, 2019, Maity 124  
*et al.*, 2022), and this introduces a timescale which is much longer than 125  
 the characteristic time scales associated with the instantaneous turbu- 126  
 lent flow structures. Numerical simulations of the laminar and turbu- 127  
 lent mixed cavity natural convection have been reported in the range 128  
 $10^5 \leq Ra \leq 5 \times 10^8$  by Fabregat and Pallares (2020) and at 129  
 $Ra = 3.6 \times 10^9$  by Lavrinenko *et al.*, (2023), where  $Ra$  is the Rayleigh 130  
 number, the ratio of buoyancy and thermal diffusivity. At such high 131  
 $Ra$ , the thermal boundary layers on the horizontal walls are fully tur- 132  
 bulent, while those attached to the thermally active vertical walls, 133  
 although unsteady, are essentially laminar. We selected this flow, for 134  
 which DNS can be obtained, as a prototypical indoor turbulent natural 135  
 convection flow in a generic room to analyze the turbulent dispersion 136  
 of particle tracers. 137

This paper is structured as follows: Sec. II describes the physical 138  
 model of the mixed cavity configuration, outlines the organization and 139  
 the challenge framework, and indicates the metrics used for the com- 140  
 parison of the results of the different participants. Section III is devoted 141  
 to the presentation and discussion of the results. Finally, conclusions 142  
 and recommendations are outlined in Sec. IV. 143

144 II. PROBLEM DEFINITION AND CHALLENGE  
145 FRAMEWORK

## 146 A. Physical model

147 We consider the dispersion of particles in a three-dimensional  
 148 turbulent natural convection flow enclosed in a room-sized cubical  
 149 cavity. The physical model of the cubical cavity, with dimension  
 150  $L = 2.5$  m, and the Cartesian coordinates adopted are shown in Fig. 1.  
 151 The origin of coordinates is located at the center of the cavity. The bot-  
 152 tom wall and a vertical wall are kept at a constant and uniform temper-  
 153 ature ( $T_H$ ), larger than the constant and uniform temperature of the  
 154 top and the vertical opposed wall ( $T_C$ ). The other two vertical sidewalls  
 155 are considered perfectly adiabatic. The fluid is air at ambient tempera-  
 156 ture ( $T_0 = (T_H + T_C)/2$ ) and pressure. The physical properties of the  
 157 fluid (see Table I) are assumed to be constant with temperature  
 158 except for the density, which varies linearly with temperature

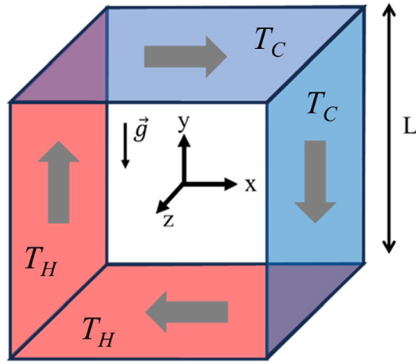


FIG. 1. Sketch of the cubical cavity and the coordinates. Hot/cold walls are indicated in red/blue. The arrows show the rotation of the large-scale flow circulation.

B. Challenge framework

The objective of the challenge is to assess the validity of using a computationally affordable turbulence model to reproduce both the flow dynamics and the dispersion of the aerosol cloud in an idealized indoor environment.

The Challenge was officially announced on October 2, 2023. A flyer, included in the supplementary material, was distributed to a mailing list of approximately 400 recipients. This list comprised researchers within the organizers' network, supplemented with emails gathered from journal publications focused on numerical simulations of turbulent natural convection flows and particle dispersion. We received expressions of interest from 30 teams. These teams were provided with the Instructions document, available in the supplementary material. By the submission deadline of May 1, 2024, data had been received from 12 teams, contributing a total of 15 simulations. Each team's results were presented and discussed during an online workshop held on June 20, 2024. Table II provides an affiliation-ordered list of participants, representing academic institutions, research centers and engineering firms.

To prevent misleading collaborations among participants, the challenge was organized as a blind test. Participants were unaware of the other teams until after the data submission deadline, and file exchanges between participants and organizers were conducted via private Google Drive folders for each team. The DNS data published by Fabregat and Pallares (2020) and by Lavrinenko et al., (2023), which were made freely available to the teams during the challenge, were recommended as benchmarks. Participants were required to submit data in ASCII or VTK formats to facilitate post-processing with the open-source multi-platform software ParaView (ParaView, 2024).

Table III summarizes the most important information from the simulations submitted. In addition, the specific details of each turbulence models used and of the models of the different terms of the particle force balance are included as supplementary material. The last column of Table III identifies each specific simulation with a code with two letters. The randomized first letter (from A to L) identifies the team, while the second corresponds to the turbulent modeling used (namely, L for large-eddy simulation, H for hybrid URANS-LES methods, S for scale-adaptive simulation, U for URANS-based simulation, or R for RANS-based simulation). Three teams (F, H, and L) performed the simulations with commercial codes, six teams (B, C, D, G, I, and K) with the open-source OpenFOAM solver, and three teams (A, E, and J) used their own in-house solvers. All the simulations were carried out with finite volume solvers, except for the in-house solvers used by teams A and J, which are based, respectively, on finite element and finite difference techniques for the spatial discretization of the governing equations. The set of fifteen simulations comprises three large-eddy simulations, four hybrid LES-RANS simulations, two scale-adaptive simulations, three URANS-based simulations, and three RANS-based simulations. The teams were instructed to conduct a grid independence test to determine the appropriate mesh resolution. The

( $\rho = \rho_0[1 - \beta(T - T_0)]$ ). This dependence is only considered in the buoyancy term according to the Boussinesq approximation. Viscous heating and radiation heat transfer are neglected.

The values of the Rayleigh number ( $Ra = g\beta(T_H - T_C)L^3/\nu\alpha$ ) and the Prandtl number ( $Pr = \nu/\alpha$ ) are  $3.6 \times 10^9$  and 0.7, respectively. In the definitions of these non-dimensional parameters,  $\alpha = \frac{k}{\rho_0 c_p}$  is the thermal diffusivity. The flow at lower Rayleigh numbers in this configuration has been analyzed by Fabregat and Pallares (2020), and some quantities at this high Rayleigh number are reported by Lavrinenko et al. (2023) and Lavrinenko et al. (2024).

We consider the unsteady dispersion of two clouds of solid spherical particles released when the turbulent natural convection flow is statistically fully developed. The initial shape of the clouds is spherical with dimension  $D_c = 0.5$  m ( $D_c^* = \frac{D_c}{L} = 0.2$ ), and particle distribution inside the clouds is uniform. Cloud#1 is located near one of the bottom corners of the cavity, where the hot horizontal and vertical walls meet, and the center of cloud#2 is located in the geometrical center of the cavity. The coordinates of the centers of the two clouds with respect to the coordinates shown in Fig. 1 are  $x_{c1} = y_{c1} = z_{c1} = -0.4L$  and  $x_{c2} = y_{c2} = z_{c2} = 0$ , respectively.

The particles are assumed to be perfectly spherical with a constant diameter ( $d_p = 0.5 \mu\text{m}$ ) and with density  $\rho_p = 1350 \text{ kg/m}^3$ . This relatively small diameter has been selected to minimize the gravitational settling of the particles. Participants were asked to compute the particle dispersion using a Lagrangian method under the one-way coupling hypothesis and according to the following requirements: The equations of particle motion had to be integrated at least during  $t^* = t \frac{\alpha \sqrt{Ra}}{L^2} = 150$  non-dimensional time units ( $t \approx 700$  s) with a proper time integration step; the number of particles in each cloud had to be larger than 1000. According to the simulations by Lavrinenko et al., (2023), for the flow conditions considered, only a few particles are expected to reach the wall and, by default, for these events, a perfect elastic rebound can be assumed.

TABLE I. Physical properties and parameters of the problem.

$Ra$	$Pr$	$\rho_0(\text{kg/m}^3)$	$\mu$ (Pa·s)	$k$ (W/m K)	$C_p$ (J/kg K)	$\beta$ (K <sup>-1</sup> )	$L$ (m)	$T_H$ (°C)	$T_C$ (°C)	$T_0$ (°C)
$3.6 \times 10^9$	0.7	1,161	$1.85 \times 10^{-5}$	$2.64 \times 10^{-2}$	1007	$3.33 \times 10^{-3}$	2.50	28.11	25.57	26.84

TABLE II. Affiliation of the participating teams. Alphabetical order.

BuildWind SRL	Belgium
CERFACS	France
Eurecat	Spain
Federal University of Uberlândia - Westmont College	Brazil - USA
FS Dynamics Portugal	Portugal
Heilbronn University of Applied Sciences	Germany
Otto von Guericke University of Magdeburg	Germany
RMIT University - The University of Sydney	Australia
Universitat Politècnica de Catalunya	Spain
University of Birmingham	UK
University of Erlangen Nuremberg - University of Maribor	Germany - Slovenia
University of Maribor	Slovenia

242 selected grids, along with the minimum and maximum grid spacings,  
243 are reported in Table III. The value of  $y^+$  corresponding to the mini-  
244 mum distance of the nodes to the horizontal walls, where the boundary  
245 layers are turbulent, is 0.3 for the DNS grid ( $\Delta x_{\min}=1.6 \times 10^{-4}$  l). For  
246 reference,  $\Delta x_{\min}=5 \times 10^{-4}$  l corresponds to  $y^+=0.9$  and  $\Delta x_{\min}=10^{-3}$   
247 l to  $y^+=1.8$ . All teams employed hexahedral elements for their  
248 meshes, except for team A, which adopted a grid composed of tetrahe-  
249 dra with two layers of prisms attached to the walls. The LES of team L  
250 used a grid of  $7 \times 10^6$  nodes, while the other two LES teams employed  
251 finer grids, with team A using  $91 \times 10^6$  nodes and team J using  $64$   
252  $\times 10^6$  nodes. The number of elements of the meshes for the hybrid  
253 simulations are about one order of magnitude smaller and ranges  
254 between 2 and  $8 \times 10^6$  nodes. SAS were performed with grids between  
255 3 and  $4 \times 10^6$  nodes. The grids selected for URANS and RANS-based  
256 simulations generally contain a moderate number of elements, ranging  
257 from 0.03 to  $4.8 \times 10^6$  nodes, except for the simulation of team F,  
258 which used  $21.2 \times 10^6$  nodes. Non-uniform grids stretched toward the  
259 walls were used by all teams, except team J, which used a uniform grid.  
260 The minimum non-dimensional grid spacings, scaled with the size of  
261 the cavity, located near the walls are of order  $10^{-4}$ – $10^{-3}$  and most of  
262 the non-dimensional maximum grid spacings, located near the center  
263 of the cavity are of order  $10^{-2}$ , with the exception of teams J and H,  
264 which used minimum grid sizes of order  $10^{-3}$ . These minimum grid  
265 spacings compare reasonably well with the DNS estimations of the  
266 time and wall-averaged temperature boundary layer thickness  
267 ( $\delta/L = (2Nu)^{-1}$ ), see for example Scheel and Schumacher, 2014) for  
268 the vertical ( $Nu_v = 78$ ,  $\delta_v/L = 6.4 \times 10^{-3}$ ) and horizontal walls  
269 ( $Nu_h = 112$ ,  $\delta_h/L = 4.4 \times 10^{-3}$ ). Also good is the estimation of the  
270 Kolmogorov length scale ( $\eta/L \approx 10^{-3}$ ) for a Rayleigh-Bénard flow at  
271  $Ra = 3.6 \times 10^9$  and  $Pr = 0.7$  (Scheel et al., 2013). The temporal dis-  
272 cretization of the governing flow equations for the LES, performed  
273 with the finer grids, is explicit (third order for team A and second  
274 order for team J), while for the hybrid, SAS and URANS simulations  
275 the discretization is implicit. The time steps employed by the different  
276 teams range from  $3.5 \times 10^{-5}$  s, for the finest grid, to  $2 \times 10^{-1}$  s for the  
277 coarser grids. The minimum number of particles per cloud was set by  
278 the organizers according to preliminary numerical tests that showed  
279 that the particle dispersion rate metrics, which are presented and

described below, in Subsec. II C, were essentially independent for 280  
clouds with 1000 or more particles. The gravity and drag forces were 281  
considered by all the teams in the particle force balance. In any case, 282  
the terminal velocity of the particles is  $10 \mu\text{m/s}$  and consequently grav- 283  
ity is not expected to play a significant role in the dispersion which is 284  
monitored during 700 s. The lift force and thermophoresis, included in 285  
the particle force balance by some teams, are also expected to have a 286  
very limited effect, because of the relatively small density ratio between 287  
the fluid and the particles and the reduced values of the temperature 288  
gradients where the particle dispersion takes place (i.e., outside the 289  
thin thermal boundary layers near the thermally active walls). Random 290  
walk models are incorporated in the motion of the particles to account 291  
for the effect of turbulence fluctuations in simulations using SAS, 292  
URANS or RANS. 293

### C. Metrics for the comparison of the results 294

Participants were asked to submit the surface averaged Nusselt 295  
numbers on the vertical ( $Nu_v$ ) and horizontal ( $Nu_h$ ) walls. These are 296  
defined as  $Nu_v = \langle q_v'' \rangle L/k(T_H - T_C)$  and  $Nu_h = \langle q_h'' \rangle L/k(T_H - T_C)$ , 297  
where  $\langle q_v'' \rangle$  and  $\langle q_h'' \rangle$  are the surface averaged wall heat fluxes on the 298  
vertical and horizontal walls, respectively. 299

The deviations, with respect to DNS, of the predictions of the 300  
velocity, temperature, and turbulence kinetic energy profiles along 301  
the wall bisectors of the vertical symmetry plane of the cavity 302  
( $z = 0$ ), were evaluated by computing the root mean squared differ- 303  
ences. First, we interpolated the data submitted by the different 304  
teams onto the DNS mesh and computed the root mean squared 305  
values as 306

$$\sigma_\phi = \sqrt{\frac{\sum_{i=1}^{i=N^{DNS}} (\phi_i^X - \phi_i^{DNS})^2}{N^{DNS}}}, \quad (1)$$

where  $\sigma_\phi$  is the rms for the quantity  $\phi$ , which can correspond to veloc- 307  
ity, temperature or turbulence kinetic energy,  $\phi_i^X$  is the data of team X 308  
interpolated onto the DNS mesh,  $\phi_i^{DNS}$  is the data corresponding to 309  
the DNS profiles and  $N^{DNS}$  is the number of grid points along the wall 310  
bisectors used in the DNS. 311

The square of the average distance, or separation, of all possible 312  
particle pairs has been used to monitor the dispersion of the two parti- 313  
cle clouds. We defined three quantities, given in Eqs. (2)–(4) to mea- 314  
sure, respectively, the three-dimensional dispersion within the cavity 315  
( $D_{xyz}^{*2}$ ), the dispersion in the plane of rotation of the large-scale circula- 316  
tion ( $D_{xy}^{*2}$ ) and the dispersion along the  $z$ -direction ( $D_z^{*2}$ ), that corre- 317  
sponds to the direction of the main alignment of the rotation vector of 318  
the large-scale flow (see Fig. 1). 319

$$D_{xyz}^{*2} = \frac{1}{N} \sum_{i,j} \left( [x_i^* - x_j^*]^2 + [y_i^* - y_j^*]^2 + [z_i^* - z_j^*]^2 \right), \quad (2)$$

$$D_{xy}^{*2} = \frac{1}{N} \sum_{i,j} \left( [x_i^* - x_j^*]^2 + [y_i^* - y_j^*]^2 \right), \quad (3)$$

$$D_z^{*2} = \frac{1}{N} \sum_{i,j} \left( [z_i^* - z_j^*]^2 \right). \quad (4)$$

In Eqs. (2) to (4),  $N$  is the total number of possible particle pairs, which 320  
is related to the total number of particles in each cloud,  $n$ , as 321

TABLE III. Summary of the simulations details.

Team	Code	Turbulence	Spatial discretization	Grid	$\Delta x_{\min}/\Delta x_{\max}$	Temporal discretization <sup>a</sup>	#particles/cloud	Particle forces	Code
A	AVBP (Schonfeld and Rudgyard, 1999; Duchaine <i>et al.</i> , 2021)	LES: WALE	Finite element. 3rd order	91M tetrahedral/prism	$2.5 \times 10^{-3}$ $2.0 \times 10^{-2}$	Explicit. 3 <sup>rd</sup> order $\Delta t_f$ $= \Delta t_p = 3.5 \times 10^{-5}$ s	2000	Drag Gravity	A-L
B	OpenFOAM 2106 (Weller <i>et al.</i> , 1998)	URANS: $k-\varepsilon$	Finite volume. 1st order upwind	0.4M hexahedral (75 × 75 × 75)	$6.0 \times 10^{-3}$ $6.2 \times 10^{-2}$	Implicit. 1st order $\Delta t_f = \Delta t_p = 10^{-1}$ s	1440	Drag Gravity Random-Walk	B-U
C	OpenFOAM 11 (Weller <i>et al.</i> , 1998)	SAS: $k-\omega$ SST	Finite volume. 2nd order	3.2M hexahedral (147 × 147 × 147)	$4.7 \times 10^{-4}$ $1.3 \times 10^{-2}$	Implicit. 1st order $\Delta t_f = 2 \times 10^{-2}$ s $\Delta t_p = 5 \times 10^{-3}$ s $\Delta t_p = 5 \times 10^{-3}$ s	1021	Drag Gravity Random-Walk	C-S
D	OpenFOAM 2112 (Weller <i>et al.</i> , 1998)	RANS: $k-\omega$	Finite volume. 2nd order	4.8M hexahedral (168 × 168 × 168)	$2.4 \times 10^{-3}$ $2.0 \times 10^{-2}$	Implicit. 1st order $\Delta t_f = \Delta t_p = 10^{-1}$ s	1000	Drag Lift Gravity Random-Walk	D-R
E	UNSCYFL3D (Velasco <i>et al.</i> , 2022)	DES: SST URANS: SST	Finite volume. 2nd order	2.0M hexahedral (125 × 125 × 125)	$8.0 \times 10^{-4}$ $5.6 \times 10^{-2}$	Implicit. 2nd order $\Delta t_f = \Delta t_p = 10^{-1}$ s	55 000	Drag Gravity Thermo-phoresis Random-Walk	E-H E-U
F	STAR-CCM+ 2022.1.1 (STAR-CCM+, 2024)	RANS: $k-\omega$ SST	Finite volume. 1st order	21.2M hexahedral (276 × 276 × 276)	$2.0 \times 10^{-3}$ $1.2 \times 10^{-2}$	$\Delta t_p = 4 \times 10^{-2}$ s	1500	Drag Gravity	F-R
G	OpenFOAM 11 (Weller <i>et al.</i> , 1998)	DES: $k-\omega$ SST	Finite volume. 2nd order	4.2M hexahedral (161 × 161 × 161)	$5.1 \times 10^{-4}$ $1.3 \times 10^{-2}$	Implicit. 1st order $\Delta t_f = \Delta t_p = 10^{-2}$ s	10 000	Drag gravity random-walk	G-H
H	Ansys Fluent, 2024R1 (Ansys Fluent, 2024)	SAS: $k-\omega$ SST SBES using LES: WALE, RANS: $k-\omega$ SST	Finite volume. 2nd order	8.0M unstructured hexahedral	$4.0 \times 10^{-4}$ $6.4 \times 10^{-3}$	Implicit. 2nd order $\Delta t_p = 10^{-2}$ s	1000	Drag gravity	G-S H-H
I	OpenFOAM 11 (Weller <i>et al.</i> , 1998)	DES: $k-\omega$ SST	Finite volume. 2nd order	1.0M hexahedral (100 × 100 × 100)	$2.8 \times 10^{-4}$ $1.7 \times 10^{-2}$	Implicit. 1st order (max. $\Delta t = 0.017$ s)	2500	Drag gravity random-walk	I-H
J	MultiFlow3D (Fraga <i>et al.</i> , 2016; Monka <i>et al.</i> , 2023)	LES: Smagorinsky	Finite difference 2nd order	64M hexahedral (400 × 400 × 400)	$2.5 \times 10^{-3}$ $2.5 \times 10^{-3}$	Explicit. 2nd order $\Delta t_f = \Delta t_p = 5 \times 10^{-3}$ s	1500	Drag gravity lift Added mass	J-L
K	OpenFOAM 8 (Weller <i>et al.</i> , 1998)	RANS: $k-\varepsilon$	Finite volume. 2nd order	0.03M (prisms + unstructured hexahedra)	$5.5 \times 10^{-3}$ $4.0 \times 10^{-2}$	$\Delta t_p = 10^{-1}$ s	1464	Drag gravity lift	K-R
L	STAR-CCM+ 2021.3 (STAR-CCM+, 2024)	LES: WALE URANS: $k-\varepsilon$	Finite volume. 2nd order	7M hexahedral (191 × 191 × 191) 2M hexahedral (126 × 126 × 126)	$8.0 \times 10^{-4}$ $7.2 \times 10^{-3}$ $8.0 \times 10^{-4}$ $1.8 \times 10^{-2}$	Implicit. 2nd order $\Delta t_f = 1.6 \times 10^{-2}$ s Implicit. 2nd order $\Delta t_f = 10^{-1}$ s	5016	Drag gravity pressure gradient	L-L L-U

<sup>a</sup> $\Delta t_f$ : Time step for the flow equations.  $\Delta t_p$ : Time step for the particle equations.

$$N = \sum_{k=1}^{n-1} (n-k) = \frac{n(n-1)}{2}. \quad (5)$$

322 According to the definitions of Eqs. (2) to (4)

$$D_{xyz}^{*2} = D_{xy}^{*2} + D_z^{*2}. \quad (6)$$

323 The limiting dimensional values of the mean squared distance,  $D_{xyz}^2$ ,  
324 corresponding to a perfectly uniform distribution of particles in a cubi-  
325 cal box, with dimension  $L$ , can be computed as

$$\begin{aligned} D_{xyz}^2(t \rightarrow \infty) &= \frac{1}{L^6} \int_{z_2=-L/2}^{z_2=L/2} \int_{y_2=-L/2}^{y_2=L/2} \int_{x_2=-L/2}^{x_2=L/2} \\ &\times \left\{ \int_{x_1=-L/2}^{x_1=L/2} \int_{y_1=-L/2}^{y_1=L/2} \int_{z_1=-L/2}^{z_1=L/2} \left[ \left\langle (x_1 - x_2)^2 + (y_1 - y_2)^2 + (z_1 - z_2)^2 \right\rangle dx_1 dy_1 dz_1 \right] \right\} \\ &dx_2 dy_2 dz_2 = \frac{L^2}{2}. \end{aligned} \quad (7)$$

326 Similarly,  $D_{xy}^2(t \rightarrow \infty) = \frac{L^2}{3}$  and  $D_z^2(t \rightarrow \infty) = \frac{L^2}{6}$ .  
327 Initially, the particles are released in spherical clouds, with diame-  
328 ter  $D_c$ , and particle distribution is uniform. The corresponding dimen-  
329 sional value of  $D_{xyz}^2$  can be computed as

$$\begin{aligned} D_{xyz}^2(t=0) &= \frac{1}{\left(\frac{\pi D_c^3}{6}\right)^2} \int_{\varphi_2=0}^{\varphi_2=2\pi} \int_{\theta_2=0}^{\theta_2=\pi} \int_{r_2=0}^{r_2=D_c/2} \\ &\times \left\{ \int_{\varphi_1=0}^{\varphi_1=2\pi} \int_{\theta_1=0}^{\theta_1=\pi} \int_{r_1=0}^{r_1=D_c/2} \left[ \left\langle (r_1 \sin \theta_1 \cos \varphi_1 - r_2 \sin \theta_2 \cos \varphi_2)^2 \right. \right. \right. \\ &+ (r_1 \sin \theta_1 \sin \varphi_1 - r_2 \sin \theta_2 \sin \varphi_2)^2 \\ &+ (r_1 \sin \theta_1 \sin \varphi_1 - r_2 \sin \theta_2 \sin \varphi_2)^2 \\ &\left. \left. \left. + (r_1 \cos \theta_1 - r_2 \cos \theta_2)^2 \right\rangle r_1^2 \sin \theta_1 dr_1 d\theta_1 d\varphi_1 \right] \right\} \\ &\times r_2^2 \sin \theta_2 dr_2 d\theta_2 d\varphi_2 = \frac{3D_c^2}{10}. \end{aligned} \quad (8)$$

330 Similarly,  $D_{xy}^2(t=0) = \frac{D_c^2}{5}$  and  $D_z^2(t=0) = \frac{D_c^2}{10}$ .  
331 These limiting dimensional values can be used to bound the non-  
332 dimensional values of the mean squared average distances between 0  
333 and 1

$$D_{xyz}^{**2} = \frac{D_{xyz}^2 - D_{xyz}^2(t=0)}{D_{xyz}^2(t \rightarrow \infty) - D_{xyz}^2(t=0)}, \quad (9)$$

$$D_{xy}^{*2} = \frac{D_{xy}^2 - D_{xy}^2(t=0)}{D_{xy}^2(t \rightarrow \infty) - D_{xy}^2(t=0)}, \quad (10)$$

$$D_z^{*2} = \frac{D_z^2 - D_z^2(t=0)}{D_z^2(t \rightarrow \infty) - D_z^2(t=0)}. \quad (11)$$

334 In this case, the following inequality holds for the non-dimensional  
335 distances,  $D_{xyz}^{*2} \neq D_{xy}^{*2} + D_z^{*2}$ .

### III. RESULTS AND DISCUSSION 336

#### A. Flow and heat transfer 337

338 **Figure 2** shows the differences, expressed as a percentage, of the  
339 predictions of the surface averaged Nusselt numbers on the horizontal  
340 and vertical walls with respect to the DNS results ( $Nu_h^{DNS} = 112$ ,  
341  $Nu_v^{DNS} = 78$ ). In general, the predictions obtained with the URANS or  
342 RANS approaches show larger deviations ( $\pm 25\%$ ) than the LES/hybrid  
343 or SAS methods ( $-12\%$ ). The two SAS simulations, carried out with  
344 similar grid resolutions, exhibit differences smaller than 5%. Four of  
345 the simulations performed with the LES/hybrid techniques (A-L, L-L,  
346 G-H, and H-H) also show deviations smaller than 5%. These simula-  
347 tions used, respectively, grids of 91, 7, 4.2, and 8 M nodes, while the  
348 simulations E-H and I-H, with differences larger than 5% were carried  
349 out with coarser meshes of 2 and 1 M nodes. The LES of team J also  
350 show differences larger than 5%, despite the use of a uniform grid with  
351 64 M nodes.

352 The time averaged profiles of the non-dimensional velocity, tem-  
353 perature, and turbulence kinetic energy along the horizontal and verti-  
354 cal bisectors of the vertical symmetry plane of the cavity are plotted in  
355 **Figs. 3–5**, respectively. The length, time, and temperature scales, used  
356 to obtain the non-dimensional variables, are the size of the cavity,  $L$ ,  
357 the convection time,  $L^2/\alpha\sqrt{Ra}$ , and the temperature increment,  
358  $T_H - T_C$  (i.e.,  $x_i^* = x_i/L$ ,  $u_i^* = u_i L^2/\alpha\sqrt{Ra}$  and  $\theta = (T - T_0)/(T_H$   
359  $- T_C)$ ). The DNS predictions are indicated using symbols and the  
360 results of the various teams using lines of different colors. The profiles  
361 of the teams that presented two simulations (E, G and L) are plotted  
362 with the same color but with a different line pattern. For clarity, we  
363 plotted LES/hybrid and SAS/URANS/RANS results separately. **Figures**  
364 **3** and **4**, corresponding to the velocity and temperature profiles,  
365 respectively, show that, overall, the predictions of the LES/hybrid sim-  
366 ulations exhibit less variability and a better agreement with the DNS.  
367 An exception is the simulation I-H, performed with a relatively coarse  
368 mesh. This simulation shows significant deviations with respect to the

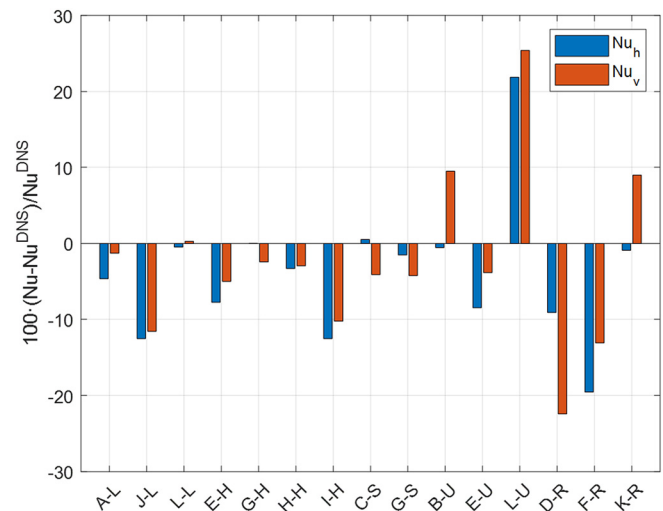


**FIG. 2.** Differences in the surface-averaged Nusselt numbers on the horizontal ( $Nu_h$ ) and vertical ( $Nu_v$ ) walls.

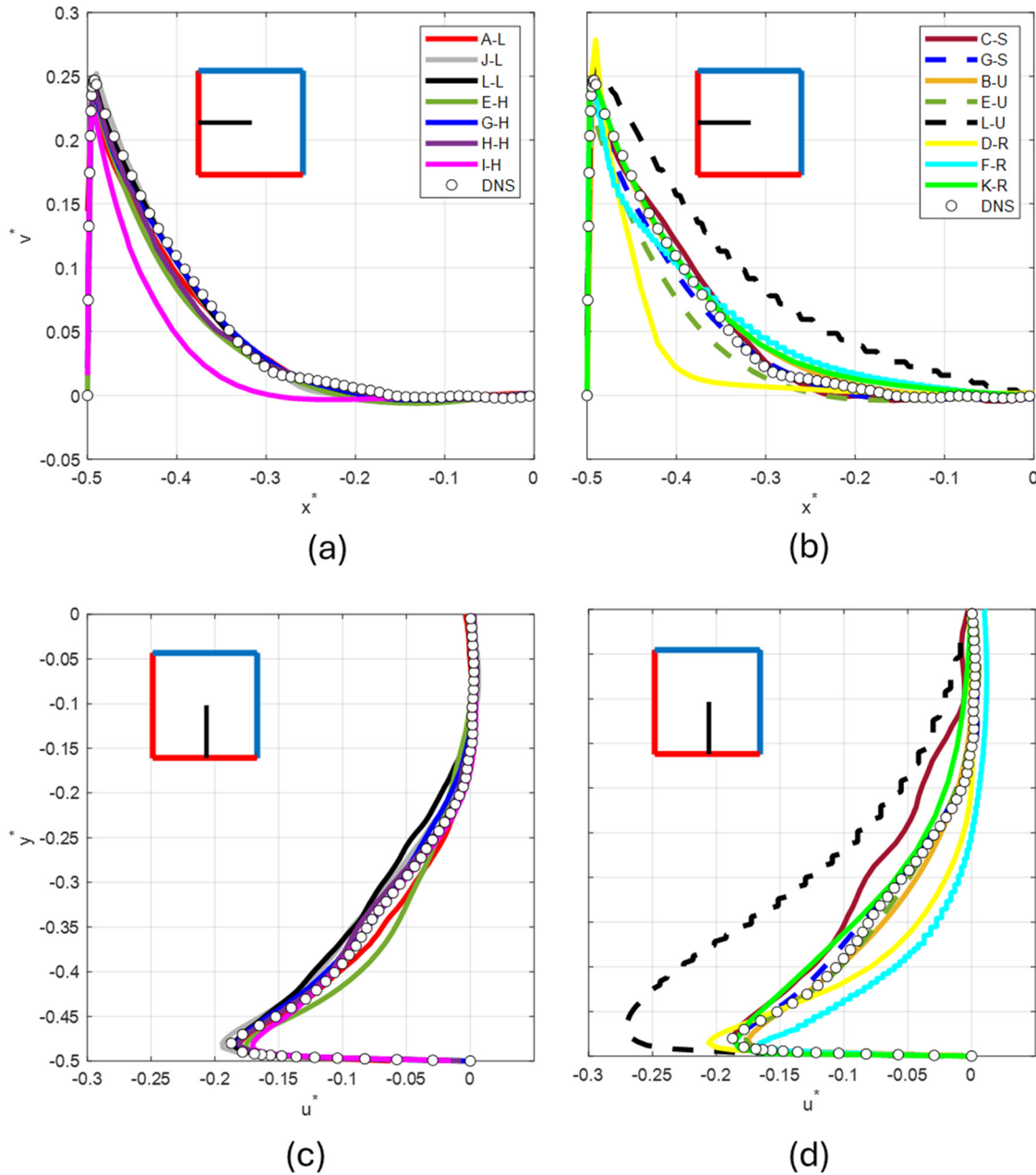


**FIG. 3.** Non-dimensional time-averaged velocity profiles along the horizontal (a) and (b) and vertical (c) and (d) bisectors of the vertical symmetry plane of the cavity ( $z = 0$ ).

369 DNS in the horizontal velocity profile of Fig. 3(a) and in the tempera-  
 370 ture profiles of Figs. 4(a) and 4(c).

371 The turbulence kinetic energy profiles, plotted in Fig. 5, also  
 372 reveal the better overall performance of LES/hybrid techniques. The  
 373 RANS simulations [Figs. 5(b) and 5(d)] tend to underpredict the intensi-  
 374 ty of the fluctuations near the wall and to overpredict them near the  
 375 center of the cavity. This is also observed for the URANS simulation  
 376 B-U, which was carried out with a relatively coarse mesh (0.4 M nodes)  
 377 and a first-order spatial discretization. The SAS results (C-S and G-S)

and the URANS, E-U, show predictions that are closer to the DNS. 378  
 We quantified the departure, from the DNS, of the profiles shown in 379  
 Figs. 3–5, by computing the root mean squared differences, defined in 380  
 Eq. (1). The values are plotted in Fig. 6(a), for the velocity and tempera- 381  
 ture profiles, and in Fig. 6(b) for the turbulence kinetic energy. These 382  
 figures summarize the differences already highlighted, when discussing 383  
 the profiles of the time-averaged velocity, temperature and turbulence 384  
 kinetic energy. Figure 6(b) indicates that LES/Hybrid techniques, along 385  
 with SAS, provide a relatively accurate prediction of the turbulence 386

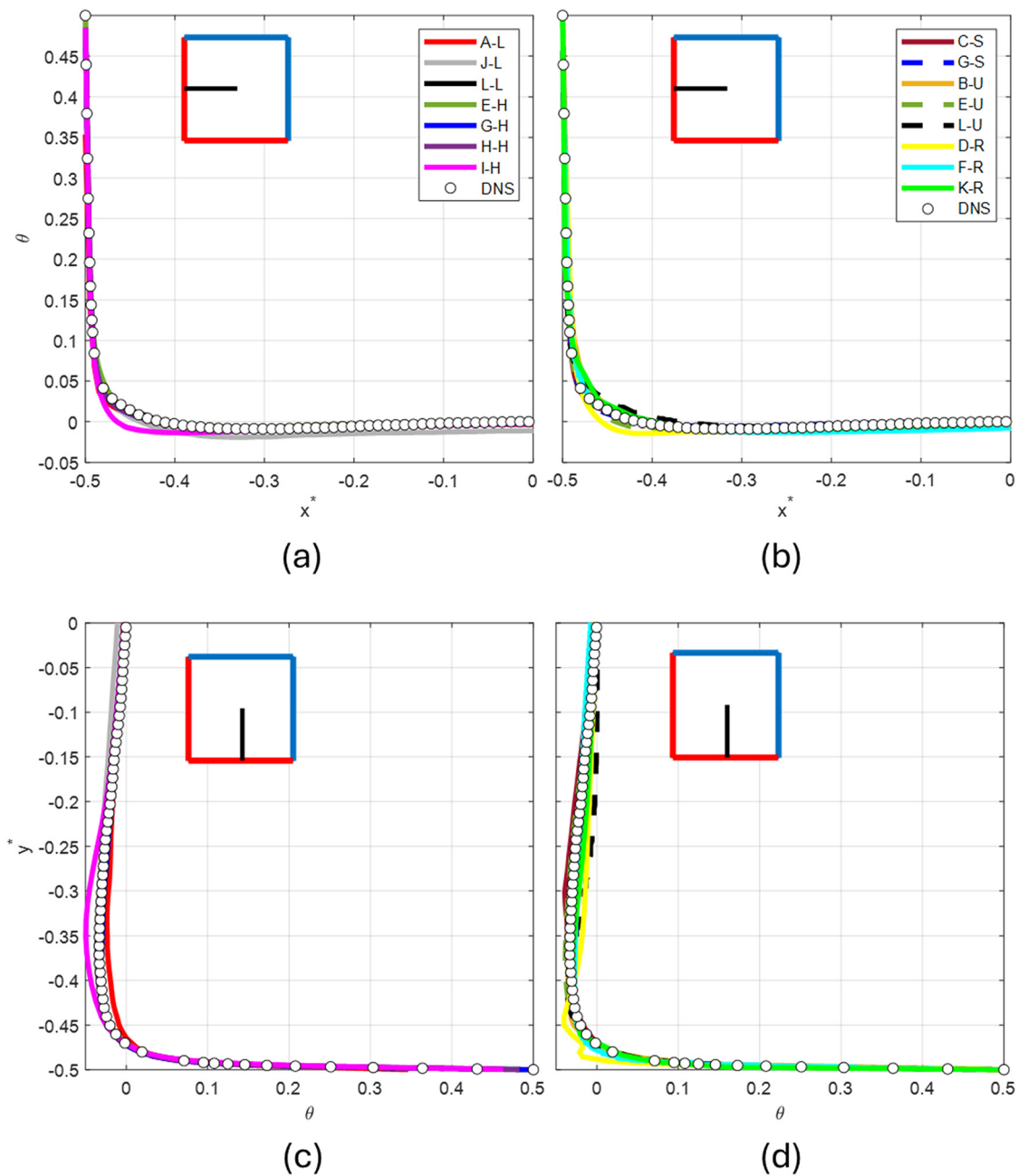


**FIG. 4.** Non-dimensional time-averaged temperature profiles along the horizontal (a) and (b) and vertical (c) and (d) bisectors of the vertical symmetry plane of the cavity ( $z = 0$ ).

387 kinetic energy, especially when compared with the RANS and  
 388 URANS methods. Exceptions are the simulation I-H, that, as  
 389 indicated above, exhibits relatively large deviations of the velocity profiles  
 390 and the URANS simulation E-U, which reproduces well the  
 391 turbulence kinetic energy [Figs. 5(b) and 5(d)] and shows moderate  
 392 differences with respect to DNS in the velocity and temperature  
 393 profiles [Figs. 6(a)].

The spatial distribution of turbulence kinetic energy within the 394  
 cavity plays a crucial role in the three-dimensional dispersion of parti- 395  
 cle clouds. To illustrate this, the two-dimensional distributions of the 396  
 turbulence kinetic energy in the vertical symmetry plane of the cavity 397  
 ( $z = 0$ ) and in the horizontal mid plane ( $y = 0$ ) are plotted in Figs. 7– 398  
 10. The initial positions of the particle clouds are indicated by the white circles 399  
 in Figs. 7(a), 8(a), 9(a) and 10(a), corresponding to the 400

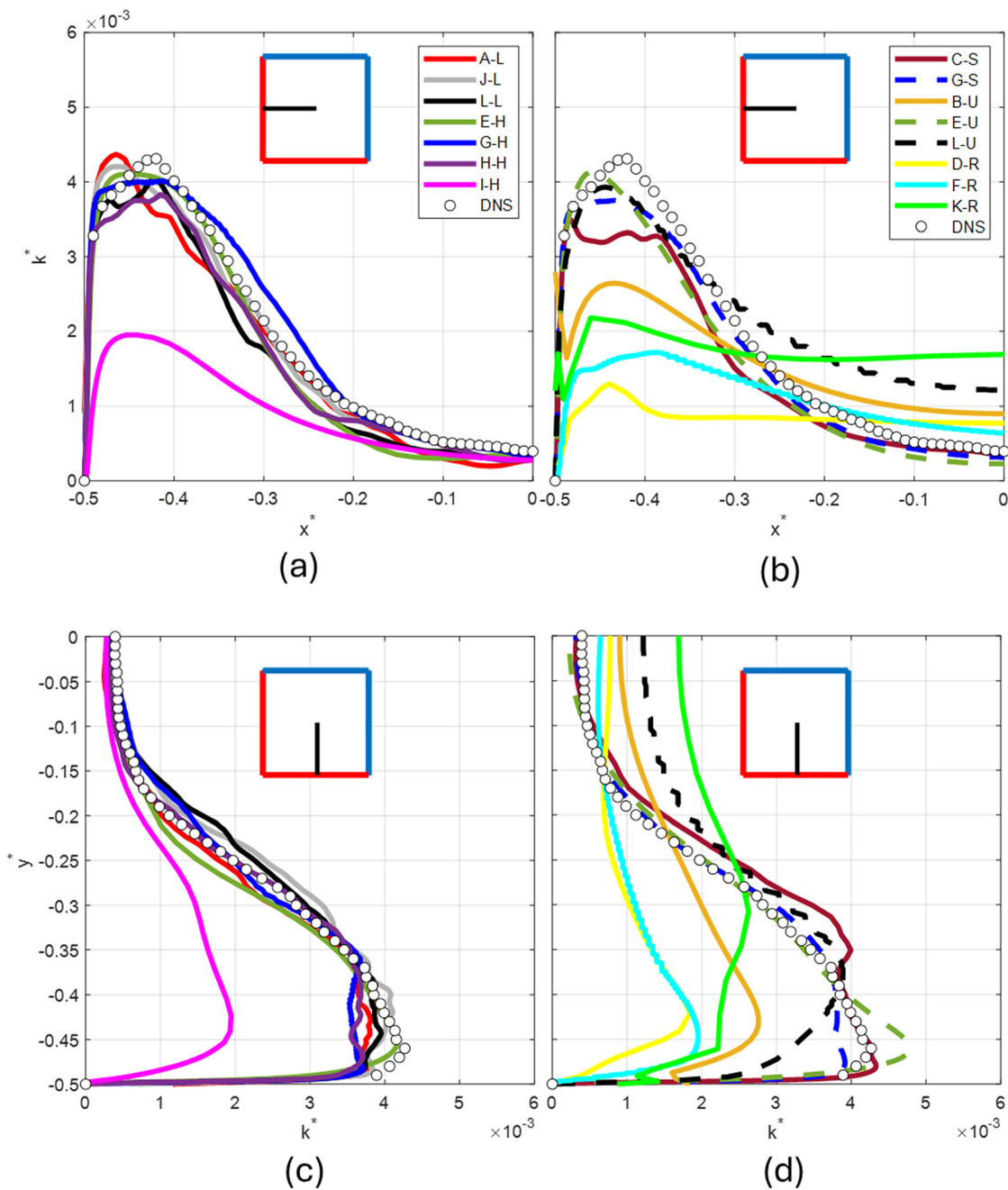
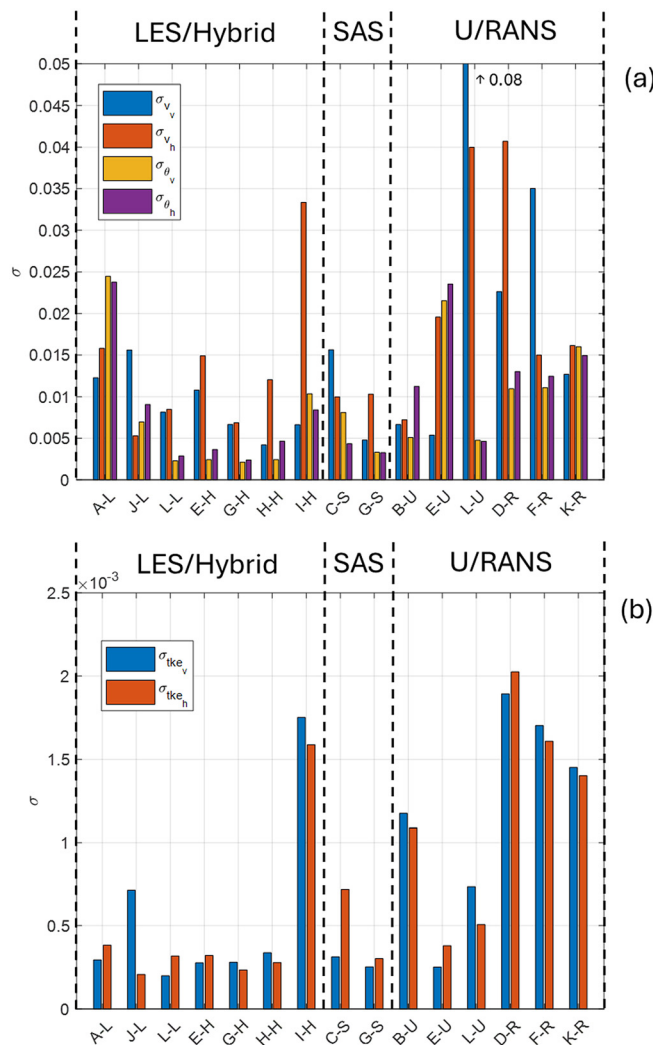


FIG. 5. Non-dimensional turbulence kinetic energy profiles along the horizontal (a) and (b) and vertical (c) and (d) bisectors of the vertical symmetry plane of the cavity ( $z = 0$ ).

401 DNS results. Cloud#1 is shown with a dashed line and Cloud#2, with a  
 402 continuous line. A local minimum in fluctuation intensities can be  
 403 observed near the center of the cavity. This area is an almost stagnant  
 404 region in terms of time-averaged behavior, as indicated by the velocity  
 405 profiles shown in Fig. 3. This is precisely where Cloud#2 originates.  
 406 The turbulence kinetic energy reaches a local maximum along the path

of large-scale flow recirculation, occurring where the time-averaged  
 velocity declines from its peak (located very close to the wall) to a local  
 minimum at the center of the cavity [see Figs. 3(a) and 5(a)]. The  
 turbulence kinetic energy exhibits localized maxima near the top left  
 and bottom right corners of the vertical symmetry plane of the cavity,  
 where the hot and cold walls meet [see, for example, Fig. 7(a)]. The



**FIG. 6.** Root mean squared differences, between the different predictions and the DNS, in the profiles of (a) velocity and temperature and (b) turbulence kinetic energy along the horizontal and vertical bisectors of the vertical symmetry plane of the cavity ( $z = 0$ ). The values of the bars above the maximum scale of the vertical axis are indicated.

The contours of the turbulence kinetic energy of the three URANS are plotted in Figs. 9(d)–9(f) and 10(d)–10(f). The simulation E-U [Figs. 9(e) and 10(e)], carried out using the  $k-\omega$  SST model and a grid of 2 M cells, agrees with the DNS while the simulation L-U [Figs. 9(f) and 10(f)], albeit sharing the same grid resolution, exhibits larger differences with respect to the DNS using the  $k-\epsilon$  model. The simulations B-U [Figs. 9(d) and 10(d)], also carried out with a  $k-\epsilon$  model but on a relatively coarse grid (0.4 M cells) shows larger deviations in the distributions of the turbulence kinetic energy with respect to the DNS. The three RANS-based simulations (D-R, F-R, and K-R) generally underpredict the levels of the turbulence kinetic energy, as shown in Figs. 9(g)–9(i) and 10(g)–10(i) irrespective of the turbulence model ( $k-\epsilon$  or  $k-\omega$ ) or grid resolution used (see Table III). Overall, the evaluation of the local turbulence kinetic energy distribution is characterized by significantly higher uncertainty in comparison with the velocity and temperature mean profiles.

In summary, the comparative study performed indicates that, in general, SAS methods predict the heat transfer rates and the time-averaged distributions of velocity, temperature, and turbulent kinetic energy as accurately as LES or hybrid techniques, provided the mesh resolutions are comparable.

### B. Particle dispersion

Under statistically fully developed flow conditions, we have considered the independent dispersion of two initially spherical particle clouds of identical size. Cloud#1 is released near one corner of the cavity and Cloud#2, in the center of the cavity (see Fig. 11, Multimedia available online). It can be seen that Cloud#1 is rapidly advected by the large-scale recirculation while particles belonging to Cloud#2 are progressively dispersed within the nearly stagnant center of the cavity and eventually are transported by the large-scale recirculation near the vertical or horizontal thermally active walls.

The time evolutions, predicted by the DNS, of the non-dimensional mean squared values of the particle separations;  $D_{xyz}^{**2}$ ,  $D_{xy}^{**2}$  and  $D_z^{**2}$ , defined in Eqs. (9)–(11), are plotted in Fig. 12. Figure 12(a) corresponds to cloud#1 and Fig. 12(b), to cloud#2. To evaluate the variability of the turbulent dispersion of the two particle clouds, we have computed the ensemble average of 40 time-evolutions (20 for each cloud) of the squared particle separations for clouds released at different times during a period of 40 non-dimensional time units. The vertical span of the shaded areas in Fig. 12 corresponds to plus/minus one standard deviation of the instantaneous mean values, which are plotted with continuous lines. The red, green and blue lines indicate the evolution of  $D_{xyz}^{**2}$ ,  $D_{xy}^{**2}$  and  $D_z^{**2}$ , respectively. In Fig. 12(a), corresponding to cloud#1, the shaded areas for the different particle separations have been indicated with the same color code (i.e., light red for  $D_{xyz}^{**2}$ , light green for  $D_{xy}^{**2}$  and light blue for  $D_z^{**2}$ ). On the other hand, for cloud#2, the time evolutions of  $D_{xyz}^{**2}$ ,  $D_{xy}^{**2}$  and  $D_z^{**2}$  as well as their standard deviations are very similar and, for clarity, in Fig. 12(b), the gray shaded area corresponds to the standard deviation of  $D_z^{**2}$ , which is the largest one.

It can be seen that the time-evolutions of the three mean squared separations of the cloud released in the center of the cavity [Fig. 12(b)] follow, on average, the same trend and reach their limiting values, corresponding to the perfectly mixed situation ( $D_{xyz}^{**2} = D_{xy}^{**2} = D_z^{**2} = 1$ ), at about 80 non-dimensional time units. Considering an average non-dimensional velocity scale of 0.1 for the large-scale circulation

distribution of the turbulence kinetic energy is essentially uniform along the  $z$  direction of the cavity, as shown in Fig. 8(a). This direction is indeed aligned to the rotation axis of the large-scale flow recirculation. As shown in Fig. 8(a), the effect of the adiabatic walls, located at  $z = -1/2$  and  $z = 1/2$ , in the distribution of the turbulence kinetic energy is restricted to areas that are very close to these walls.

Figures 7 and 8 show that, globally, the LES/hybrid techniques provide predictions of the turbulence kinetic energy spatial distributions in the  $z = 0$  (Fig. 7) and  $y = 0$  (Fig. 8) planes that closely match the DNS benchmark case. However, simulation I-H underpredicts, in general, the level of the fluctuations along the path of the large-scale flow recirculation [see Figs. 7(h) and 8(h)]. The predictions of the SAS, shown in Figs. 9(b), 9(c), 10(b), and 10(c) agree well with the DNS.

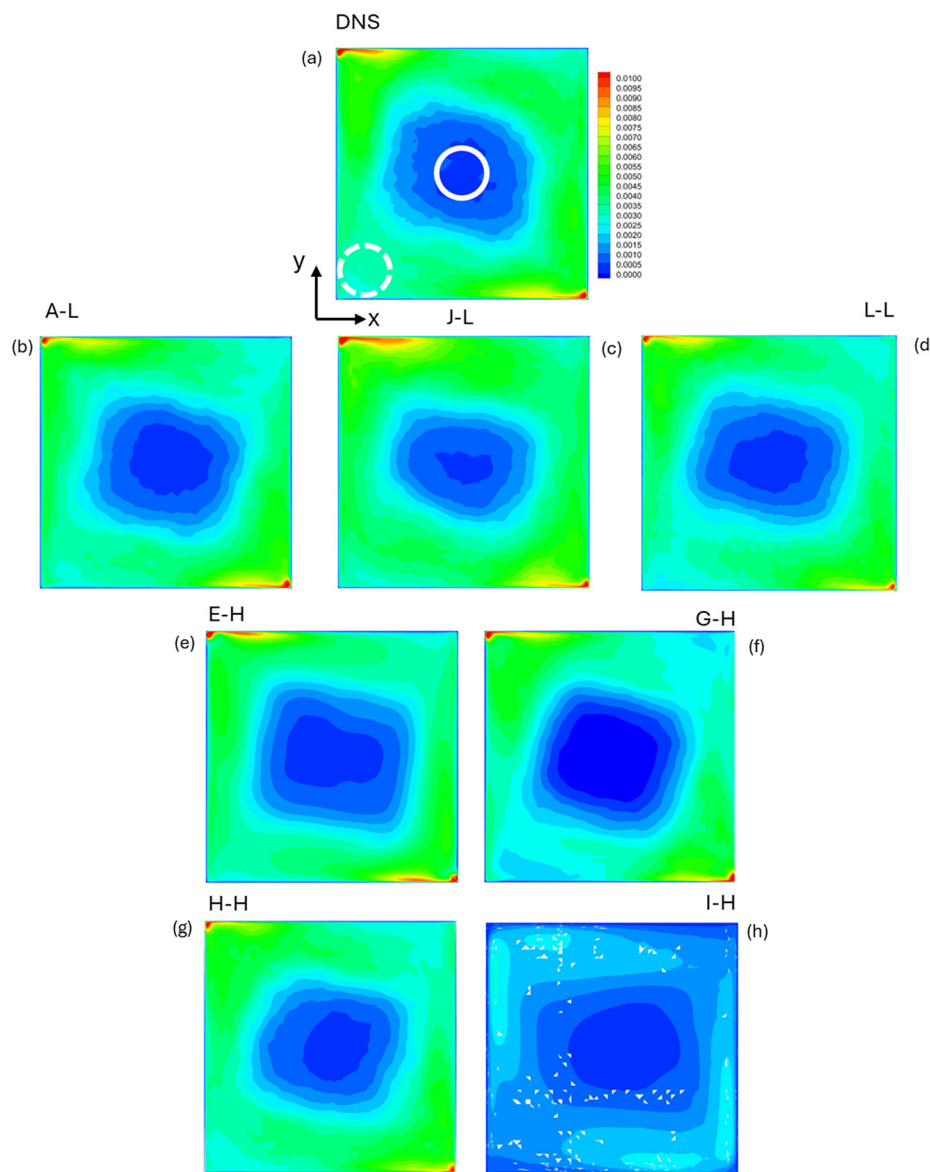


FIG. 7. Contours of the turbulence kinetic energy on the vertical symmetry plane of the cavity ( $z = 0$ ).

482 (see. Figure 3). Such a span corresponds to approximately two large-  
 483 eddy turnover times. In contrast, the time evolutions of the separations  
 484 of the particles released near one corner of the cavity [cloud#1,  
 485 Fig. 12(a)] behave distinctly. While the mean separation within the plane  
 486 of the large-scale circulation,  $D_{xy}^{**2}$ , reaches the value of a perfectly uniform  
 487 particle distribution, relatively fast (at about 40 non-dimensional  
 488 time units), the mean separation of the particles along the  $z$  direction  
 489 increases, for  $t^* > 10$ , at a lower rate and reaches the limiting value only  
 490 at  $t^* \approx 100$ . This indicates a more effective mixing within the plane of  
 491 the large-scale circulation than along the  $z$  direction. Note also that the  
 492 release of cloud#2 in the geometric center of the cavity is more effective  
 493 for dispersing particles along the  $z$  direction than the release of cloud#1  
 494 near the bottom of one lateral adiabatic wall, relatively far from the

opposite adiabatic lateral wall. Figure 12(a) shows an overshoot of the  
 time evolution of  $D_{xy}^{**2}$  at  $t^* \approx 5$ . This time corresponds to that required  
 by the fastest transported particles (namely those transported by the  
 large-scale recirculation) to reach the top wall of the cavity and bend  
 toward the horizontal direction (see Fig. 11, Multimedia available  
 online). This change in direction produces a temporary reduction of the  
 mean particle distance observed in the time evolution of  $D_{xy}^{**2}$ , and to a  
 lesser extend in the time-evolution of  $D_{xyz}^{**2}$ . In contrast, the time-  
 evolutions of cloud#2 [Fig. 12(b)] show monotonic increases in the  
 mean squared distances. Figure 12(a) shows that the largest variability  
 associated with the mean separations is observed for the time-evolutions  
 of  $D_z^{**2}$  indicating that within the large-scale circulation the fluctuations  
 along the  $z$  direction is more intermittent compared with those in the  $x$

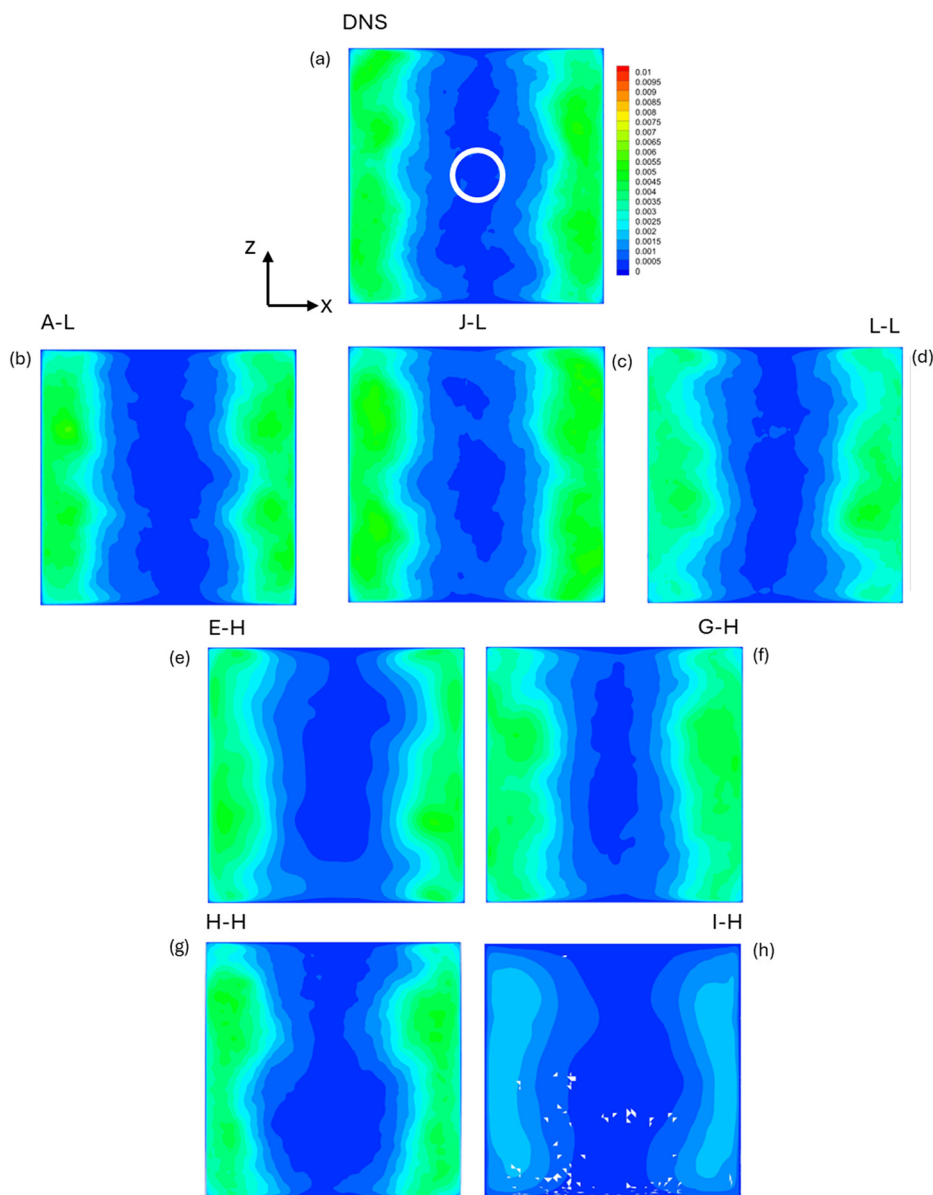


FIG. 8. Contours of the turbulence kinetic energy on the horizontal mid plane of the cavity ( $y = 0$ ).

508 or  $y$  directions. The variabilities of the distances  $D_{xyz}^{**2}$  and  $D_{xy}^{**2}$  for  
 509 cloud#1 are similar and comparable with those for cloud#2.

510 The comparisons between the time-evolutions of the mean separations of the different simulations with the mean values predicted by  
 511 the DNS are plotted in Figs. 13–17. We grouped the plots according to the simulation technique used: Fig. 13 corresponds to LES, Fig. 14 to  
 512 hybrid methods, Fig. 15 to SAS, Fig. 16 to URANS, and Fig. 17 to RANS.

513 Figure 13 shows that LES correctly predicts the dispersion of both  
 514 clouds and that the times at which the mean distances reach the limiting  
 515 values are comparable with those of DNS (i.e.,  $D_{xyz}^{**2} = D_{xy}^{**2}$   
 516  $= D_z^{**2} = 1$  for  $t^* \rightarrow \infty$ ). In contrast, the time evolution provided by

520 the hybrid simulations, E-H, H-H and I-H, plotted in Fig. 14, reaches  
 521 larger (E-H and H-H) or lower (I-H) limiting values in comparison  
 522 with the theoretical ones, which are equal to unity. This can be attrib-  
 523 uted to non-uniform final distribution of the particles within the cavity  
 524 attained at large times for these three simulations. For example, if par-  
 525 ticles tend to accumulate near the adiabatic walls, then the value of  $D_z^{**2}$   
 526 at large times will be larger than the theoretical one, ( $D_z^{**2}(t \rightarrow \infty) = \frac{1}{6}$ ) and, thus,  $D_z^{**2}(t \rightarrow \infty)$  will be higher than one  
 527 (see, for example, Fig. 14(b).E-H). Conversely, if particles tend to accu-  
 528 mulate near the center of the cavity, then  $D_z^{**2}(t \rightarrow \infty) < 1$   
 529 (Fig. 14(b).I-H). On the other hand, the simulation G-H predicts cor-  
 530 rectly the time-evolutions of the different mean separations for the two  
 531

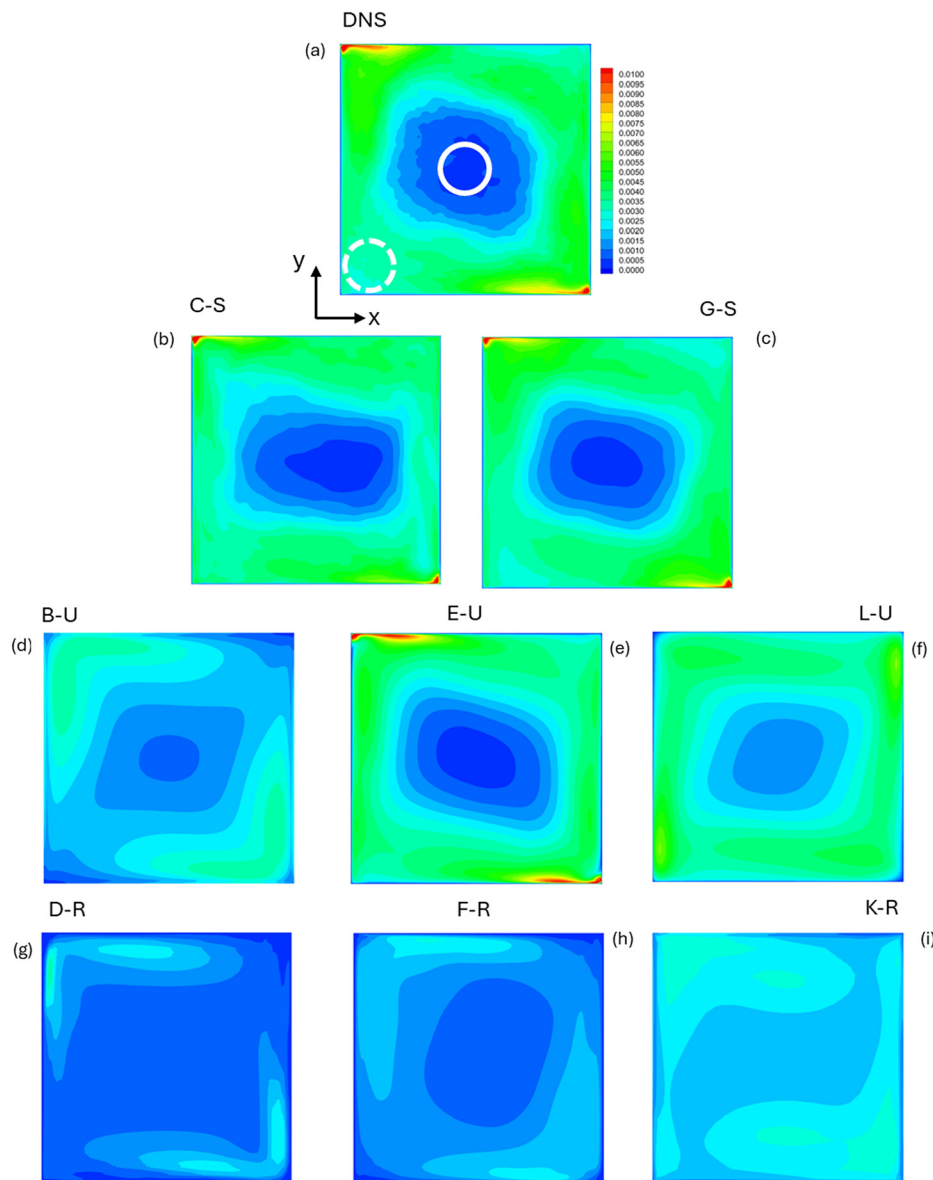


FIG. 9. Contours of the turbulence kinetic energy on the vertical symmetry plane of the cavity ( $z = 0$ ).

clouds, as shown in Figs. 14(a).G-H and 14(b).G-H. From the information reported in Table III, it is difficult to infer the reason behind the better prediction of this hybrid simulation in comparison with simulations E-H, H-H, and I-H. However, inspecting the deviations, with respect to DNS, of the time-averaged velocity, temperature, and turbulence kinetic profiles shown in Fig. 6, reveals that, except for simulation I-H, the hybrid simulations (E-H, G-H, H-H) show similar deviations of the turbulence kinetic energy [Fig. 6(b)] but the velocity and temperature profiles of simulation G-H agree better with the DNS than those corresponding to simulations E-H, H-H, and I-H.

The time evolutions of the particle distances predicted by the two SAS are plotted in Fig. 15. Both simulations are within the variability

of the dispersion of cloud#1 provided by the different DNS realizations. For cloud#2 [Figs. 15(b).C-S and 15(b).G-S] the dispersion is slightly underpredicted in the case of the simulation C-S while the simulation G-S agrees very well with the DNS. This agreement is also observed for the turbulence kinetic energy distributions shown in Figs. 9(b), 9(c), 10(b), and 10(c).

Figure 16 shows that the URANS simulation E-U reproduces the DNS fairly well, reaching a limiting value of the particle distances that is slightly larger than one. In contrast, simulations B-U and L-U and the three RANS simulations, plotted in Fig. 17, show significant deviations with respect to the DNS. In particular, these simulations underpredict the rate of dispersion of the particle clouds and this agrees with the low

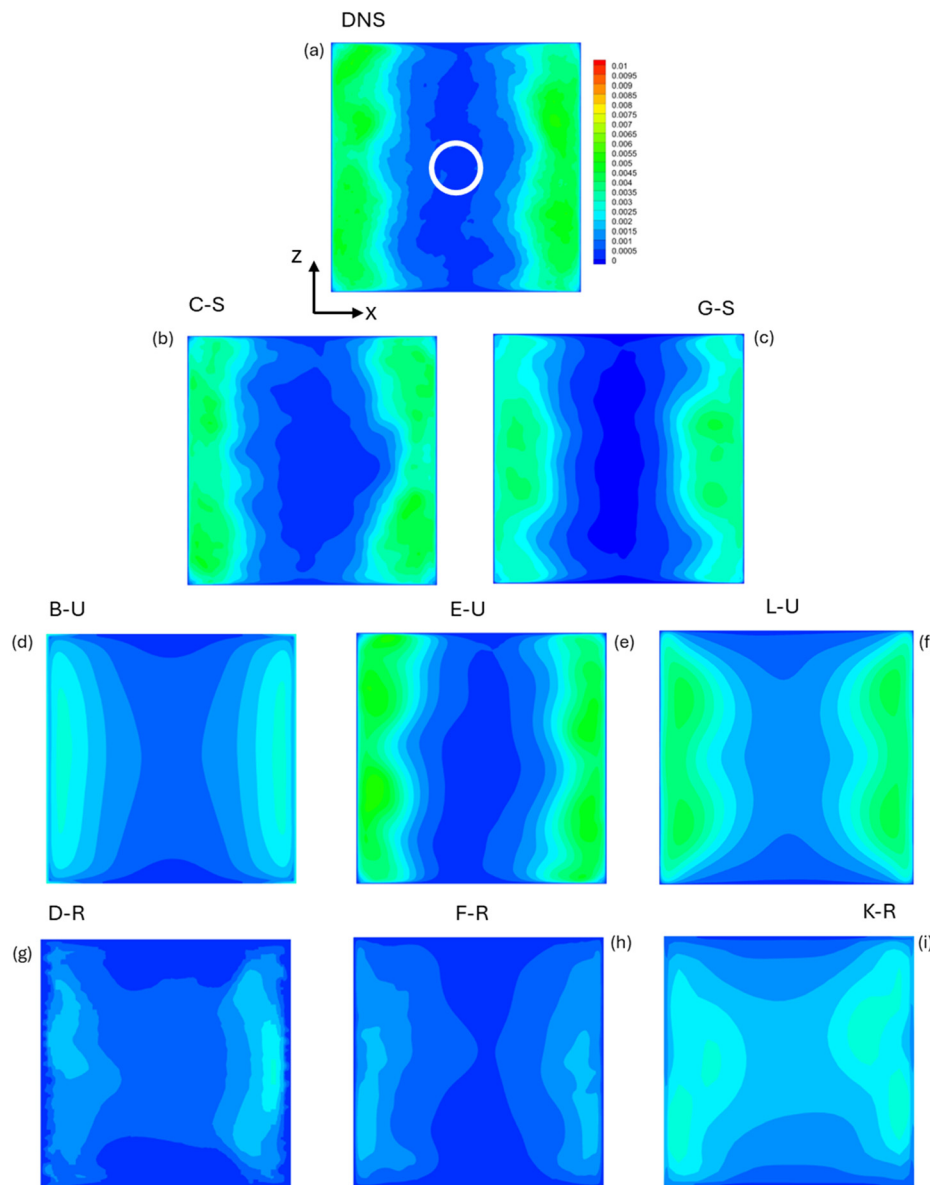


FIG. 10. Contours of the turbulence kinetic energy on the horizontal mid plane of the cavity ( $y = 0$ ).

556 levels of turbulence kinetic energy obtained by the URANS and RANS  
 557 simulations as shown in Figs. 9 and 10. These figures show that the simu-  
 558 lation E-U predicts correctly the turbulence kinetic energy distribu-  
 559 tion while the other RANS (simulations D-R, F-R, and K-R) and URANS  
 560 (B-U and L-U) systematically underestimate the overall turbulence level  
 561 of the flow [see, for example, Figs. 9(d), 9(f), 9(g), 9(h), and 9(i)].

562 Lagrangian particle dispersion in hybrid methods and URANS/  
 563 RANS flow simulations usually is performed employing stochastic  
 564 models to incorporate the effect of the instantaneous turbulent fluctua-  
 565 tions of the flow in the equations of particle motion (Mofakham and  
 566 Ahmadi, 2020; Lo et al., 2022). These models, often referred to as ran-  
 567 dom walk models (RWMs), extract the fluctuating velocity from the

mean flow solution to include the effect of the turbulent flow in the  
 568 particle path. Commonly, simulations of turbulent flows using  
 569 URANS and RANS techniques adopt the square root of the turbulence  
 570 kinetic energy as the velocity scale to compute the fluctuating compo-  
 571 nent of the particle velocity, which has been advected according to the  
 572 time-averaged velocity field. For the flow conditions considered here,  
 573 the turbulence kinetic energy peaks near the wall attaining non-  
 574 dimensional values roughly equal to  $4 \times 10^{-3}$  (see Fig. 5). This yields a  
 575 non-dimensional velocity scale for the fluctuations of approximately  
 576 0.06. This relatively large value, together with the insensitivity of most  
 577 of the RWM implemented in commercial and open-source CFD codes  
 578 to the direction of the fluctuations, can lead to an overestimation of  
 579

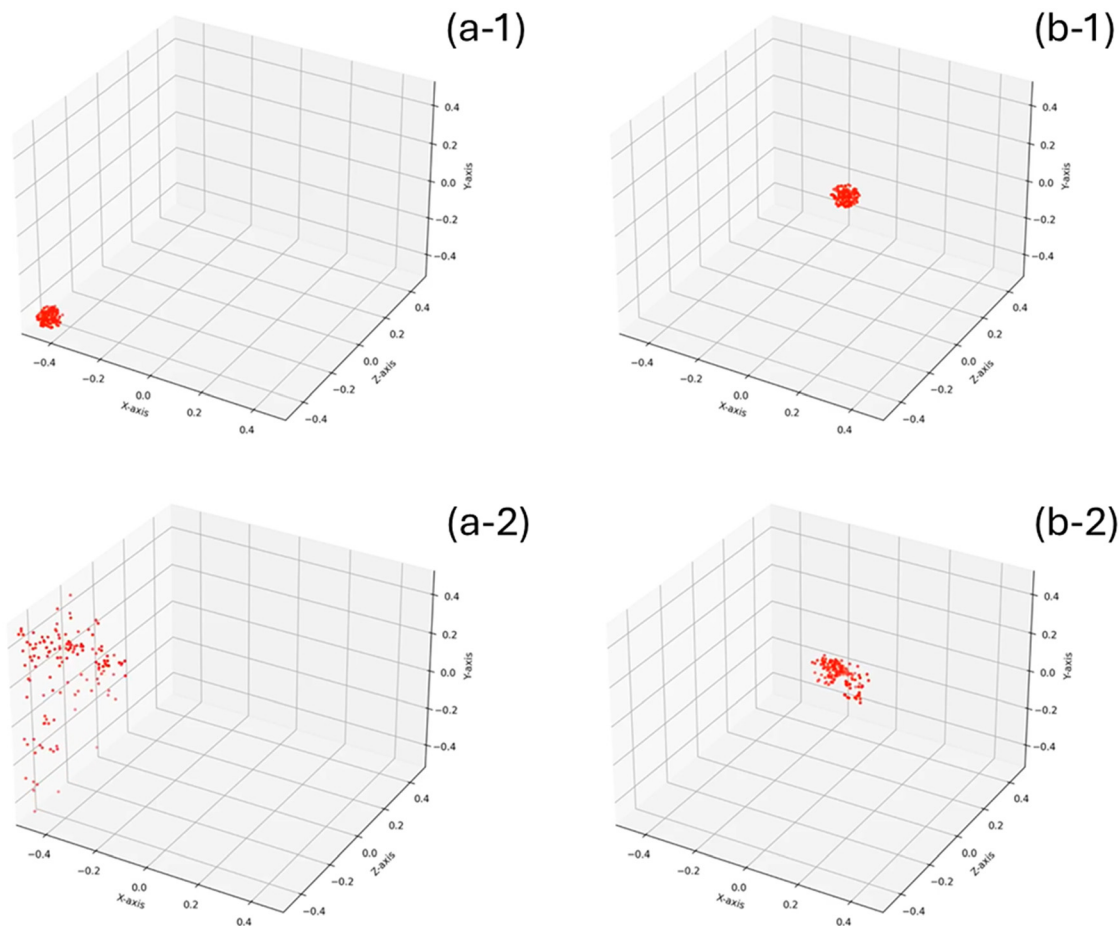


FIG. 11. Time evolution of the dispersion of the particles. (a) Cloud#1. (b) Cloud#2. (a-1) and (b-1) correspond to  $t^* = 0$  and (a-2) and (b-2) to  $t^* = 5$ . Multimedia available online.

580 the particle velocity fluctuations toward the wall, artificially increasing  
 581 particle-wall collisions and the injection of the particles very near the  
 582 wall, where the particles get trapped due to the low mean velocity and  
 583 turbulence kinetic energy. This scenario can lead to increased particle  
 584 concentrations near the walls and produce deviations from the per-  
 585 fectly uniform distribution of particles within the cavity predicted by  
 586 the DNS at large times ( $t^* > 100$ ) and expected in view of the small  
 587 Stokes number of the particles ( $St = \frac{\rho_p d_p^2 V}{18\mu L} \sim 10^{-8}$ ).

588 To quantify the differences between the averaged values provided  
 589 by the DNS and the predictions of  $D_{xyz}^{**2}$ ,  $D_{xy}^{**2}$ , and  $D_z^{**2}$  of the different  
 590 simulations, we use the deviation parameter,  $\Phi$ , which was computed  
 591 as follows. For each time evolution of  $D_{xyz}^{**2}$ ,  $D_{xy}^{**2}$ , or  $D_z^{**2}$ , we identified  
 592 the values that lay above the mean value plus one standard deviation  
 593 of the DNS (reference DNS value, hereinafter). For these values we  
 594 computed the absolute value of the difference with respect to the refer-  
 595 ence DNS value. The same procedure was then adopted for the values  
 596 below the mean value minus one standard deviation of the DNS.  
 597 Finally, the deviation parameter for the  $i$ -th mean squared separation

(i.e.,  $i \equiv xyz, xy$  or  $z$ ) of the simulation  $j$ -th is defined as the averaged 598  
 value of such differences 599

$$\Phi = \left\langle \text{abs} \left[ (D_i^{**2}(t))^j - (D_i^{**2}(t))^{DNS} \right] \right\rangle \quad (12)$$

if 600

$$\begin{aligned} (D_i^{**2}(t))^j &> (D_i^{**2}(t))^{DNS} + \sigma(D_i^{**2}(t))^{DNS} \\ \text{or } (D_i^{**2}(t))^j &< (D_i^{**2}(t))^{DNS} - \sigma(D_i^{**2}(t))^{DNS}, \end{aligned}$$

where  $\sigma(D_i^{**2}(t))^{DNS}$  is the standard deviation of the  $i$ -th mean 601  
 squared separation predicted by the DNS. Figure 18 shows the devia- 602  
 tion parameter for the three different mean particle distances of the 603  
 two clouds and for the different simulations. The LES and hybrid sim- 604  
 ulations, in general, perform better than the RANS simulations. The 605  
 exception is the simulation I-H, which shows significant differences, 606  
 with respect to the DNS of the turbulence kinetic energy [see, for 607  
 example, Fig. 8(h)]. Remarkably, the predictions of the SAS, C-S and 608

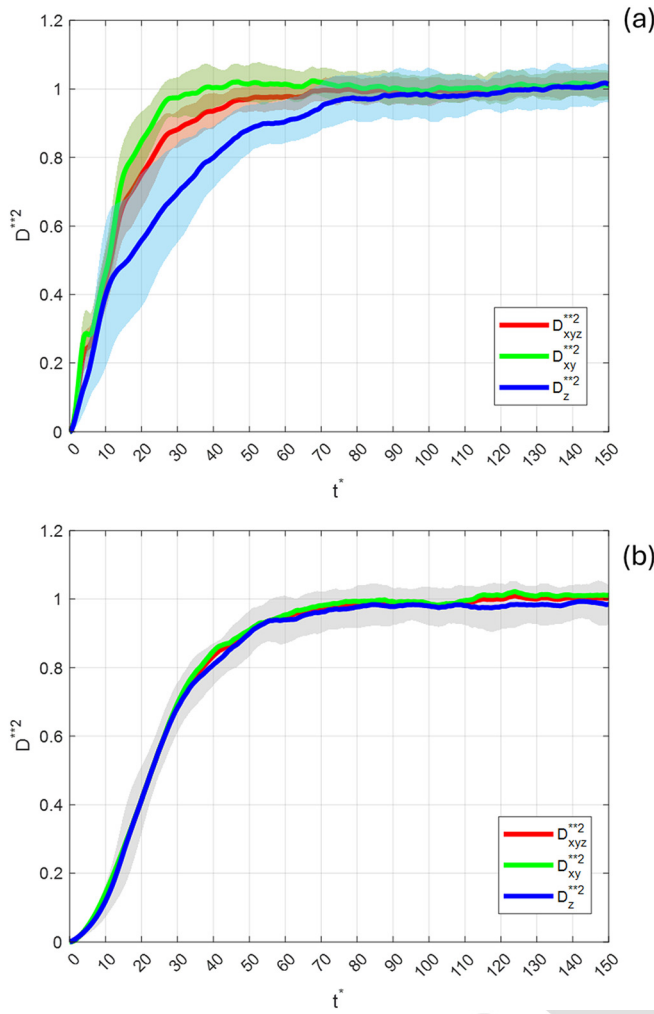


FIG. 12. Ensemble average time-evolutions of the non-dimensional mean squared particle separations. (a) Cloud#1. (b) Cloud#2.

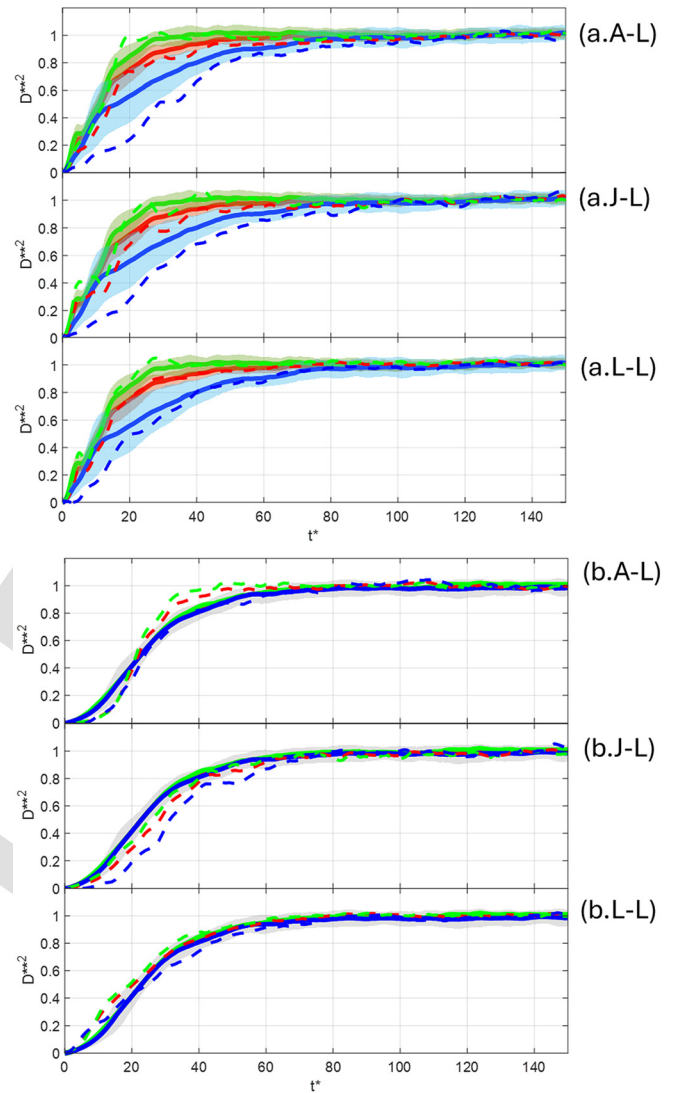


FIG. 13. Comparison LES/DNS of the time-evolutions of the non-dimensional mean squared particle separations. Red:  $D_{xyz}^{**2}$ . Green:  $D_{xy}^{**2}$ . Blue:  $D_z^{**2}$ . (a) Cloud#1. (b) Cloud#2.

609 G-S are also very close to the DNS, and they perform even better, in  
 610 some cases, than some LES and hybrid simulations. The agreement  
 611 with the DNS of the dispersion predicted by the URANS simulations  
 612 depends strongly on the prediction of the turbulence kinetic energy  
 613 distribution. For example, the simulation E-U with a similar distribu-  
 614 tion of the turbulence kinetic energy as the DNS [see Fig. 10(e)] is  
 615 characterized by a lower deviation parameter than the simulations B-U  
 616 and L-U. We recall here that the grid resolutions of these three  
 617 URANS simulations are 0.4 M nodes for B-U and 2 M nodes for E-U  
 618 and L-U and also that the turbulence models used are  $k-\varepsilon$  for B-U  
 619 and L-U and  $k-\omega$  for E-U (see Table III). This suggests that the better per-  
 620 formance of the simulation E-U can be attributed to the combination  
 621 of an adequate grid resolution together with the use of the  $k-\omega$  turbu-  
 622 lence model.

623 To summarize the comparison of the different simulations, we  
 624 plotted in Fig. 19 the differences, with respect to DNS, of the

information shown in two previous figures: Fig. 6, corresponding to the  
 deviations of the profiles of velocity, temperature, and turbulence  
 kinetic energy and Fig. 18, corresponding to the deviations of the particle  
 dispersion. For each simulation, we have averaged the four bars of  
 Fig. 6(a), the two bars of Fig. 6(b) and the six bars of Fig. 18, scaling  
 the resulting averaged values with the mean for all the simulations.  
 These scaled deviations are plotted in Fig. 19 and are accompanied by  
 three bars. The blue bar indicates jointly the differences in the velocity  
 and temperature profiles, the red bar corresponds to the differences in  
 the turbulence kinetic energy and the orange bar to the difference in  
 the particle dispersion. It can be seen that, in general, significant deviations  
 of the turbulence kinetic energy leads to relatively large deviations  
 of the particle dispersion. The exception is the simulation L-U

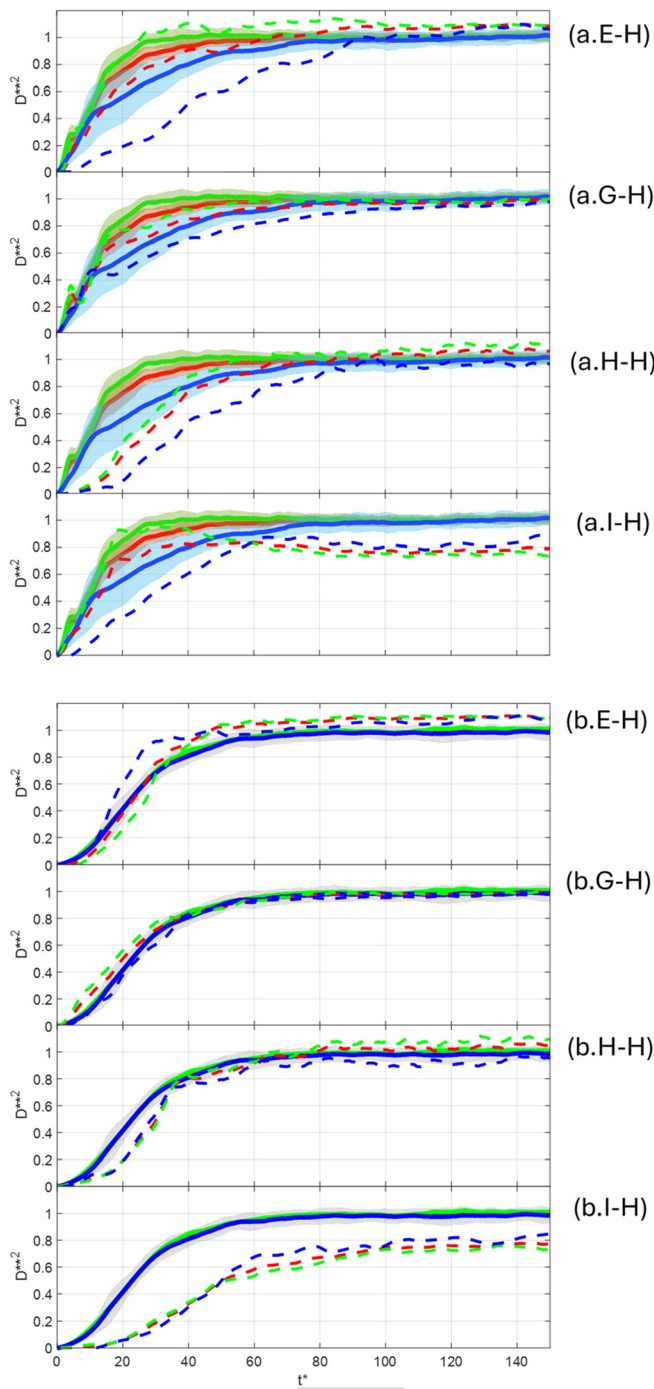


FIG. 14. Comparison hybrid simulations/DNS of the time-evolutions of the non-dimensional mean squared particle separations. Red:  $D_{xyz}^{**2}$ . Green:  $D_{xy}^{**2}$ . Blue:  $D_z^{**2}$ . (a) Cloud#1. (b) Cloud#2.

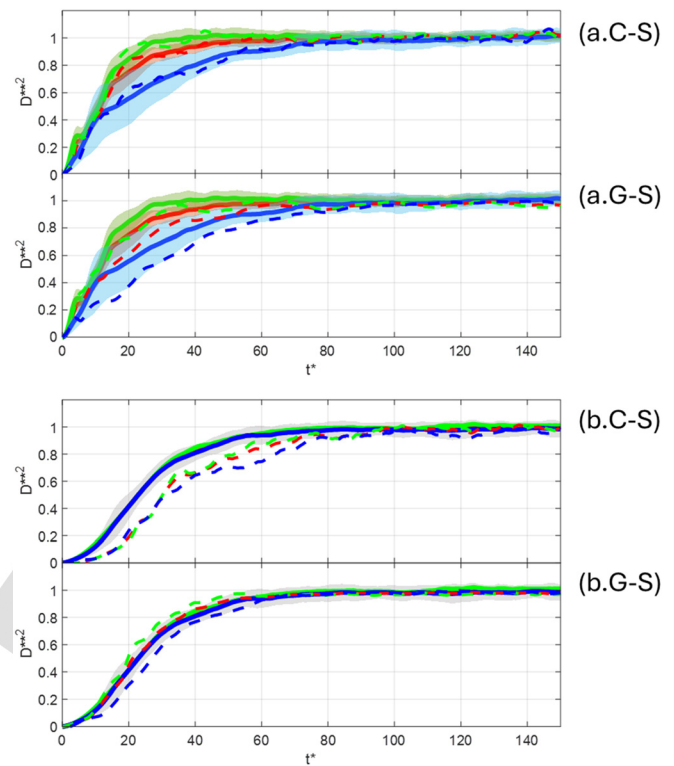


FIG. 15. Comparison SAS/DNS of the time-evolutions of the non-dimensional mean squared particle separations. Red:  $D_{xyz}^{**2}$ . Green:  $D_{xy}^{**2}$ . Blue:  $D_z^{**2}$ . (a) Cloud#1. (b) Cloud#2.

10(f)]. The differences in the velocity and temperature profiles are not strongly correlated with the differences in the particle dispersion. For example, simulations A-L and E-U show differences in the velocity and temperature profiles but predict reasonably well the cloud dispersion.

#### IV. CONCLUSIONS

In this paper, we presented and discussed the outcomes of a benchmark study conducted within the framework of an International CFD challenge. The study aimed to assess the performance of various numerical and turbulence modeling techniques to simulate the turbulent free convection flow and the dispersion of particles within a room-sized enclosure. Twelve research teams have contributed to the challenge and individually conducted a total of fifteen simulations of the same flow configuration, for which a reference direct numerical simulation (DNS) is available. The database generated consists of three large-eddy simulations (LES), four hybrid LES/RANS (Reynolds-Averaged Navier-Stokes) simulations, two Scale Adaptive Simulations (SAS), three unsteady Reynolds-averaged Navier-Stokes (URANS) simulations, and three RANS simulations. Results of the mean flow quantities and metrics of the dispersion of two clouds of particles are compared with each other and with the DNS results.

The mean flow quantities, the surface averaged Nusselt numbers, time-averaged velocity and temperature profiles, and the turbulence kinetic energy are, in general, well reproduced by the LES and the

which shows good agreement with the DNS when comparing the turbulence kinetic energy profiles [Figs. 5(b) and 5(d)] but shows substantial differences when considering the spatial distributions of the turbulence kinetic energy [compare, for example, Figs. 10(a) and

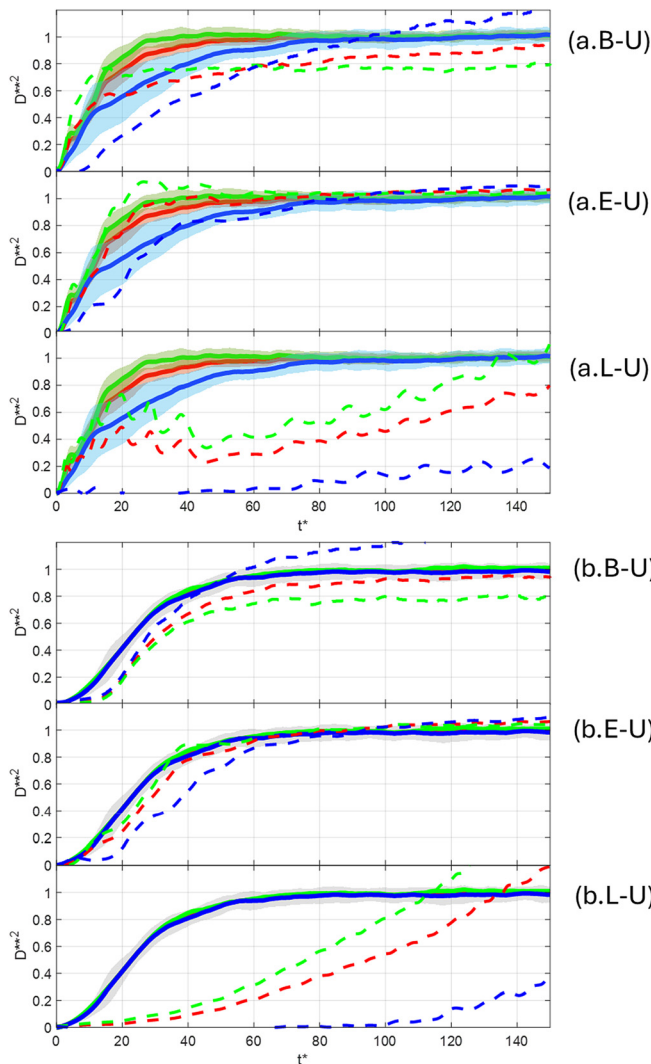


FIG. 16. Comparison URANS/DNS of the time-evolutions of the non-dimensional mean squared particle separations. Red:  $D_{xyz}^{**2}$ . Green:  $D_{xy}^{**2}$ . Blue:  $D_z^{**2}$ . (a) Cloud#1. (b) Cloud#2.

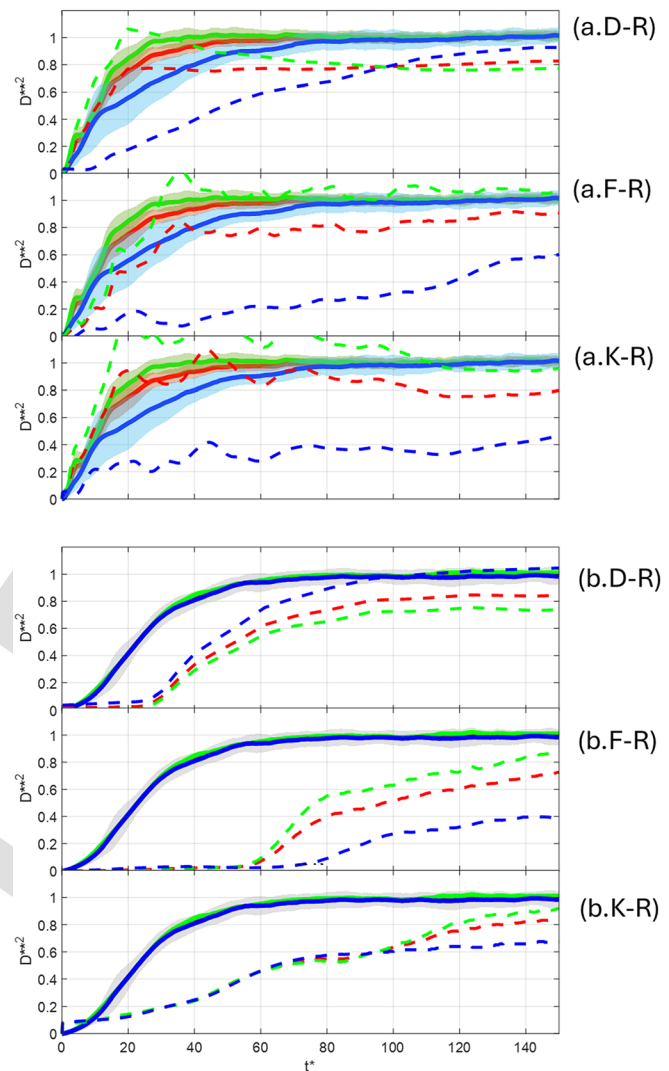


FIG. 17. Comparison RANS/DNS of the time-evolutions of the non-dimensional mean squared particle separations. Red:  $D_{xyz}^{**2}$ . Green:  $D_{xy}^{**2}$ . Blue:  $D_z^{**2}$ . (a) Cloud#1. (b) Cloud#2.

666 hybrid methods. In the case of different simulations performed with  
 667 hybrid methods the grid resolution seems to be the cause for signifi-  
 668 cant deviations when the grid is too coarse: In particular, this is  
 669 observed for simulations performed with less than 2M nodes while  
 670 simulations carried out with 2M nodes or more show much better  
 671 agreement with the DNS. The two SAS simulations performed with  
 672 similar grid resolutions as the hybrid simulations both show relatively  
 673 small deviations, comparable with those provided by the LES or the  
 674 hybrid simulations. The comparison of the three URANS cases shows  
 675 that the one performed with the  $k-\omega$  turbulence model has a better  
 676 agreement with DNS than the one carried out with the same grid reso-  
 677 lution (2M nodes) but using the  $k-\epsilon$  model. The third URANS simu-  
 678 lation, carried out with less than a quarter of the number of grid nodes  
 679 used by the other two and using the  $k-\epsilon$  model, shows larger deviations

680 from DNS, as expected. The RANS simulations also exhibit significant  
 681 differences with respect to DNS, independent of the grid resolution  
 682 and the specific turbulence model ( $k-\epsilon$  or  $k-\omega$ ) used.

683 The accuracy of particle dispersion predictions is primarily influ-  
 684 enced by the combination of the turbulence model and grid resolution,  
 685 as the choice of these factors plays a crucial role in accurately repro-  
 686 ducing the turbulence kinetic energy. In fact, LES, hybrid simulations  
 687 and URANS that properly predict the spatial distribution of the turbu-  
 688 lence kinetic energy are found to capture the time evolutions of the  
 689 mean squared separation of the particles, and, thus, the particle disper-  
 690 sion, in good agreement with DNS. Conversely, RANS simulations  
 691 and coarse-grid hybrid simulations that underpredict the overall tur-  
 692 bulance intensity of the flow, underpredict the rate of dispersion of the

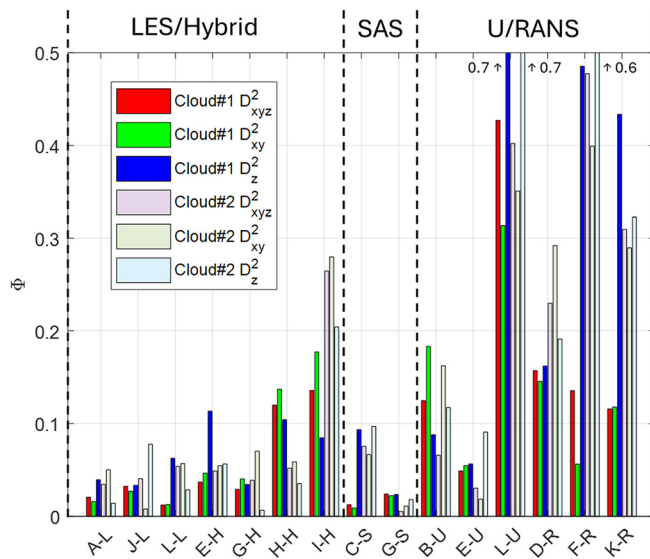


FIG. 18. Differences of the time evolutions of the mean squared particle separations predicted by the different simulations and the DNS.

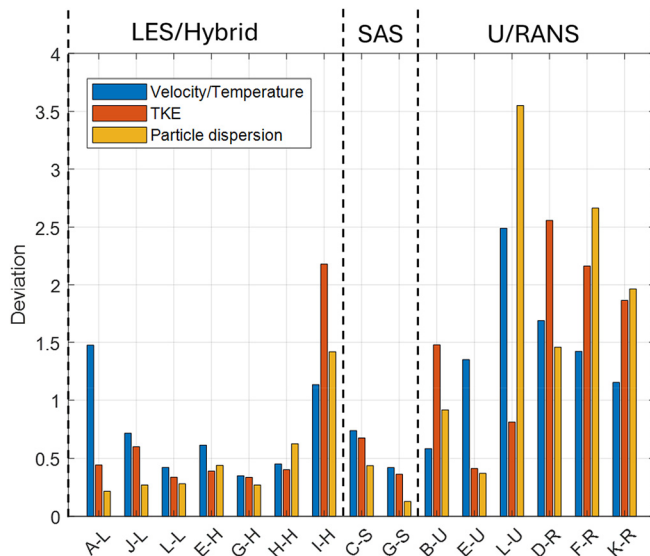


FIG. 19. Deviations, with respect to the DNS, of the time-averaged velocity/temperature fields, the turbulent kinetic energy and the particle dispersion.

ACKNOWLEDGMENTS

702

B.F. and A.M. acknowledge the use of ARCHER2 UK National Supercomputing Service. (<https://www.archer2.ac.uk>).

D.F.F. and K.I. acknowledge the use of the National Computational Infrastructure (NCI) which is supported by the Australian Government and accessed through the Sydney Informatics Hub HPC Allocation Scheme, which is supported by the Deputy Vice-Chancellor (Research), University of Sydney.

F.D. and S.S. acknowledge the access to the HPC resources of Curie/Irene Rome from TGCC under the allocation A0162A06074 made by GENCI.

J.N. acknowledges funding by the MWK Baden-Württemberg (ref. no. 32-7545.20/4/59 Mittelbauprogramm).

J.P., A.F., A.L., and S.C. acknowledge the financial funding of projects PID2020-113303GB-C21 and PID2023-146648NB-C21, funded by the Spanish Ministerio de Ciencia e Innovación and the Agencia Estatal de Investigación and the support of the Departament de Recerca i Universitats de la Generalitat de Catalunya under project. 2021SGR00732.

AUTHOR DECLARATIONS

Conflict of Interest

The authors have no conflicts to disclose.

Author Contributions

**Jordi Pallares:** Conceptualization (equal); Funding acquisition (equal); Investigation (equal); Resources (equal); Supervision (equal); Validation (equal); Writing – original draft (equal); Writing – review & editing (equal). **Bruno Fraga:** Data curation (equal); Investigation (equal); Validation (equal); Writing – review & editing (equal). **Aleksandra Monka:** Data curation (equal); Investigation (equal); Validation (equal); Writing – review & editing (equal). **Manuel Martínez:** Data curation (equal); Investigation (equal); Validation (equal); Writing – review & editing (equal). **Naomi Mestre-Curto:** Data curation (equal); Investigation (equal); Validation (equal); Writing – review & editing (equal). **Francisco Jose de Souza:** Data curation (equal); Investigation (equal); Validation (equal); Writing – review & editing (equal). **Douglas Fontes:** Data curation (equal); Investigation (equal); Validation (equal); Writing – review & editing (equal). **Natalie Jüngling:** Data curation (equal); Investigation (equal); Validation (equal); Writing – review & editing (equal). **Jennifer Niessner:** Data curation (equal); Investigation (equal); Validation (equal); Writing – review & editing (equal). **Robert Castilla:** Data curation (equal); Investigation (equal); Validation (equal); Writing – review & editing (equal). **Mercè Garcia Vilchez:** Data curation (equal); Investigation (equal); Validation (equal); Writing – review & editing (equal). **Alexandre Fabregat:** Conceptualization (equal); Data curation (equal); Investigation (equal); Supervision (equal); Validation (equal); Writing – original draft (equal); Writing – review & editing (equal). **David F. Fletcher:** Data curation (equal); Investigation (equal); Validation (equal); Writing – review & editing (equal). **Kiao Inthavong:** Data curation (equal); Investigation (equal); Validation (equal); Writing – review & editing (equal). **Matjaz Hribersek:** Data curation (equal); Investigation (equal); Validation (equal); Writing – review & editing (equal). **Paul Steinmann:** Data curation (equal); Investigation (equal); Validation (equal); Writing – review & editing

693 particle clouds, and fail in capturing, for the flow conditions considered, the ultimate perfectly uniform distribution of the particles within the cavity.

696 SUPPLEMENTARY MATERIAL

697 See the [supplementary material](#) for the details of the turbulence models employed in the simulations, as well as information about the models used for the various terms in the particle force balance.

757 (equal). **Jana Wedel**: Data curation (equal); Investigation (equal);  
 758 Validation (equal); Writing – review & editing (equal). **Florent**  
 759 **Duchaine**: Data curation (equal); Investigation (equal); Validation  
 760 (equal); Writing – review & editing (equal). **Shriram Sankurantripati**:  
 761 Data curation (equal); Investigation (equal); Validation (equal);  
 762 Writing – review & editing (equal). **Leo Amari**: Data curation (equal);  
 763 Investigation (equal); Validation (equal); Writing – review & editing  
 764 (equal). **Gábor Janiga**: Data curation (equal); Investigation (equal);  
 765 Validation (equal); Writing – review & editing (equal). **Cristian**  
 766 **Marchioli**: Conceptualization (equal); Methodology (equal); Resources  
 767 (equal); Supervision (equal); Validation (equal); Writing – original  
 768 draft (equal); Writing – review & editing (equal). **Akim Lavrinenko**:  
 769 Conceptualization (equal); Data curation (equal); Investigation (equal);  
 770 Validation (equal); Writing – review & editing (equal). **Salvatore Cito**:  
 771 Conceptualization (equal); Methodology (equal); Resources (equal);  
 772 Supervision (equal); Validation (equal); Writing – original draft  
 773 (equal); Writing – review & editing (equal). **Nelson Marques**: Data  
 774 curation (equal); Investigation (equal); Validation (equal); Writing –  
 775 review & editing (equal). **Bruno Santos**: Data curation (equal);  
 776 Investigation (equal); Validation (equal); Writing – review & editing  
 777 (equal). **Gabriele Mosca**: Data curation (equal); Investigation (equal);  
 778 Validation (equal); Writing – review & editing (equal). **Pedro Obando**  
 779 **Vega**: Data curation (equal); Investigation (equal); Validation (equal);  
 780 Writing – original draft (equal). **Jure Ravnik**: Data curation (equal);  
 781 Investigation (equal); Validation (equal); Writing – review & editing  
 782 (equal). **Nejc Vovk**: Data curation (equal); Investigation (equal);  
 783 Validation (equal); Writing – review & editing (equal).

784

785 **DATA AVAILABILITY**

786 The data that support the findings of this study are available from  
 787 the corresponding author upon reasonable request.

788 **REFERENCES**

789 Ai, Z. T. and Melikov, A. K., “Airborne spread of expiratory droplet nuclei  
 790 between the occupants of indoor environments: A review,” *Indoor air* **28**(4),  
 791 500–524 (2018).  
 792 See <https://www.ansys.com/products/fluids/ansys-fluent> for “Ansys Fluent”  
 793 (2024).  
 794 Bournel, P. E. and Boulard, T., “Effect of ventilator configuration on the distrib-  
 795 uted climate of greenhouses: A review of experimental and CFD studies,”  
 796 *Comput. Electron. Agric.* **74**(2), 195–217 (2010).  
 797 Bourouiba, L., “Fluid dynamics of respiratory infectious diseases,” *Annu. Rev.*  
 798 *Biomed. Eng.* **23**(1), 547–577 (2021).  
 799 Caciolo, M., Stabat, P., and Marchio, D., “Numerical simulation of single-sided  
 800 ventilation using RANS and LES and comparison with full-scale experiments,”  
 801 *Build. Environ.* **50**, 202–213 (2012).  
 802 Choi, H., Kim, H., and Kim, T., “Long-term simulation for predicting indoor air  
 803 pollutant concentration considering pollutant distribution based on concept of  
 804 CRPS index,” in *Building Simulation* (Tsinghua University Press, 2019), Vol.  
 805 12, pp. 1131–1140.  
 806 Concilio, C., Benito, P. A., Ramírez, C. P., and Viccione, G., “CFD simulation  
 807 study and experimental analysis of indoor air stratification in an unventilated  
 808 classroom: A case study in Spain,” *Heliyon* **10**, e32721 (2024).  
 809 Cuce, E., Sher, F., Sadiq, H., Cuce, P. M., Guclu, T., and Besir, A. B., “Sustainable  
 810 ventilation strategies in buildings: CFD research,” *Sustainable Energy Technol.*  
 811 *Assess.* **36**, 100540 (2019).  
 812 Dehbi, A., Kalilainen, J., Lind, T., and Auvinen, A., “A large eddy simulation of  
 813 turbulent particle-laden flow inside a cubical differentially heated cavity,”  
 814 *J. Aerosol Sci.* **103**, 67–82 (2017).

Delort-Laval, M., Soucasse, L., Rivière, P., and Soufiani, A., “Rayleigh–Bénard **815**  
 convection in a cubic cell under the effects of gas radiation up to  $Ra = 10^9$ ,” *Int.*  
 816 *J. Heat Mass Transfer* **187**, 122453 (2022).  
 817 Demou, A. D. and Grigoriadis, D. G., “Direct numerical simulations of Rayleigh–  
 818 Bénard convection in water with non-Oberbeck–Boussinesq effects,” *J. Fluid*  
 819 *Mech.* **881**, 1073–1096 (2019).  
 820 Duchaine, F., Cizeron, C. N., Odier, N., Dombard, J., Marchall, S., Francois, N.,  
 821 and Poinso, T., “High-performance CFD for respiratory droplet turbulent dis-  
 822 persion in a ventilated city bus,” *Int. J. Comput. Fluid Dyn.* **35**(9), 758–777  
 823 (2021).  
 824 Fabregat, A. and Pallares, J., “Heat transfer and boundary layer analyses of lami-  
 825 nar and turbulent natural convection in a cubical cavity with differently heated  
 826 opposed walls,” *Int. J. Heat Mass Transfer* **151**, 119409 (2020).  
 827 Fraga, B., Stoesser, T., Lai, C. C., and Socolofsky, S. A., “A LES-based Eulerian–  
 828 Lagrangian approach to predict the dynamics of bubble plumes,” *Ocean*  
 829 *Modell.* **97**, 27–36 (2016).  
 830 Gilani, S., Montazeri, H., and Blocken, B., “CFD simulation of stratified indoor  
 831 environment in displacement ventilation: Validation and sensitivity analysis,”  
 832 *Build. Environ.* **95**, 299–313 (2016).  
 833 Hanjalić, K. and Vasić, S., “Computation of turbulent natural convection in rect-  
 834 angular enclosures with an algebraic flux model,” *Int. J. Heat Mass Transfer*  
 835 **36**(14), 3603–3624 (1993).  
 836 Jones, A. P., “Indoor air quality and health,” *Atmos. Environ.* **33**(28), 4535–4564  
 837 (1999).  
 838 Kalilainen, J., Rantanen, P., Lind, T., Auvinen, A., and Dehbi, A., “Experimental  
 839 investigation of a turbulent particle-laden flow inside a cubical differentially  
 840 heated cavity,” *J. Aerosol Sci.* **100**, 73–87 (2016).  
 841 Lavrinenko, A., Fabregat, A., Gisbert, F., and Pallares, J., “Direct numerical simu-  
 842 lation of pathogen-laden aerosol dispersion in buoyancy-driven turbulent flow  
 843 within confined spaces,” *Int. Commun. Heat Mass Transfer* **152**, 107272  
 844 (2024).  
 845 Lavrinenko, A., Gisbert, F., Pallares, J., and Fabregat, A., “Fully-resolved numeri-  
 846 cal simulations of the turbulent flow and particle deposition in a cubical cavity  
 847 with two pairs of differentially heated opposed walls at Rayleigh number  
 848  $3.6 \times 10^9$ ,” *Int. Commun. Heat Mass Transfer* **141**, 106564 (2023).  
 849 Li, Y. and Nielsen, P. V., “CFD and ventilation research,” *Indoor Air* **21**(6), 442–  
 850 453 (2011).  
 851 Li, Z., Wen, Q., and Zhang, R., “Sources, health effects and control strategies of  
 852 indoor fine particulate matter (PM<sub>2.5</sub>): A review,” *Sci. Total Environ.* **586**,  
 853 610–622 (2017).  
 854 Lo, C., Bons, J., Yao, Y., and Capecehatro, J., “Assessment of stochastic models for  
 855 predicting particle transport and deposition in turbulent pipe flows,” *J. Aerosol*  
 856 *Sci.* **162**, 105954 (2022).  
 857 Maity, P., Koltai, P., and Schumacher, J., “Large-scale flow in a cubic  
 858 Rayleigh–Bénard cell: Long-term turbulence statistics and Markovianity of  
 859 macrostate transitions,” *Philos. Trans. R. Soc. London, Ser. A* **380**(2225),  
 860 20210042 (2022).  
 861 Maroni, M., Seifert, B., and Lindvall, T., *Indoor Air Quality: A Comprehensive*  
 862 *Reference Book* (Elsevier, 1995).  
 863 Mofakham, A. A. and Ahmadi, G., “On random walk models for simulation of  
 864 particle-laden turbulent flows,” *Int. J. Multiphase Flow* **122**, 103157 (2020).  
 865 Monka, A., Fraga, B., Soper, D., and Hemida, H., “Influence of thermal stratifica-  
 866 tion on the transport of polydispersed expiratory particles,” *Phys. Fluids*  
 867 **35**(10), 103304 (2023).  
 868 See <https://www.paraview.org/> for “Paraview” (2024).  
 869 Riley, W. J., McKone, T. E., Lai, A. C., and Nazaroff, W. W., “Indoor particulate  
 870 matter of outdoor origin: Importance of size-dependent removal mechanisms,”  
 871 *Environ. Sci. Technol.* **36**(2), 200–207 (2002).  
 872 Salat, J., Xin, S., Joubert, P., Sergeant, A., Penot, F., and Le Quere, P.,  
 873 “Experimental and numerical investigation of turbulent natural convection in a  
 874 large air-filled cavity,” *Int. J. Heat Fluid Flow* **25**(5), 824–832 (2004).  
 875 Scheel, J. D. and Schumacher, J., “Local boundary layer scales in turbulent  
 876 Rayleigh–Bénard convection,” *J. Fluid Mech.* **758**, 344–373 (2014).  
 877 Scheel, J. D., Emran, M. S., and Schumacher, J., “Resolving the fine-scale structure  
 878 in turbulent Rayleigh–Bénard convection,” *New J. Phys.* **15**(11), 113063 (2013).  
 879 Schönfeld, T. and Rudgyard, M., “Steady and unsteady flow simulations using the  
 880 hybrid flow solver AVBP,” *AIAA J.* **37**(11), 1378–1385 (1999).  
 881

- 882 Seguel, J. M., Merrill, R., Seguel, D., and Campagna, A. C., "Indoor air quality,"  
883 *Am. J. Lifestyle Med.* **11**(4), 284–295 (2017).
- 884 Sheikhejad, Y., Aghamolaei, R., Fallahpour, M., Motamedi, H., Moshfeghi, M.,  
885 Mirzaei, P. A., and Bordbar, H., "Airborne and aerosol pathogen transmission  
886 modeling of respiratory events in buildings: An overview of computational fluid  
887 dynamics," *Sustainable Cities Soc.* **79**, 103704 (2022).
- 888 Shen, C., Gao, N., and Wang, T., "CFD study on the transmission of indoor pollu-  
889 tants under personalized ventilation," *Build. Environ.* **63**, 69–78 (2013).
- 890 Shim, G., Narayanan, S. R., and Yang, S., "Numerical simulation of virus-laden  
891 aerosol transmission in real human respiratory airways," *Phys. Fluids* **35**(10),  
892 101903 (2023).
- 893 Soucasse, L., Podvin, B., Rivière, P., and Soufiani, A., "Proper orthogonal decom-  
894 position analysis and modelling of large-scale flow reorientations in a cubic  
895 Rayleigh–Bénard cell," *J. Fluid Mech.* **881**, 23–50 (2019).
- 896 See [https://www.plm.automation.siemens.com/global/en/products/simcenter/  
897 STAR-CCM.html](https://www.plm.automation.siemens.com/global/en/products/simcenter/STAR-CCM.html) for "STAR-CCM+" (2024).
- AQ2 898 Tan, Z. and Zhang, Y., "An overview of particulate matter in indoor environ-  
899 ments: Sources and effects," *ASHRAE Trans.* **109**, 89–100 (2003).
- 900 Teimurazov, A., Reiter, P., Shishkina, O., and Frick, P., "Heat transport in a cell  
901 heated at the bottom and the side," *Europhys. Lett.* **134**(3), 34001 (2021).
- 902 Tric, E., Labrosse, G., and Betrouni, M., "A first incursion into the 3D struc-  
903 ture of natural convection of air in a differentially heated cubic cavity, from  
904 accurate numerical solutions," *Int. J. Heat Mass Transfer* **43**(21), 4043–4056  
905 (2000).
- 906 van Hooff, T., Blocken, B., and Tominaga, Y., "On the accuracy of CFD simula-  
907 tions of cross-ventilation flows for a generic isolated building: Comparison of  
908 RANS, LES and experiments," *Build. Environ.* **114**, 148–165 (2017).
- Vasiliev, A., Frick, P., Kumar, A., Stepanov, R., Sukhanovskii, A., and Verma, M. 909  
K., "Transient flows and reorientations of large-scale convection in a cubic 910  
cell," *Int. Commun. Heat Mass Transfer* **108**, 104319 (2019). 911
- Velasco, L. J., Venturi, D. N., Fontes, D. H., and de Souza, F. J., "Numerical simu- 912  
lation of drag reduction by microbubbles in a vertical channel," *Eur. J. Mech. B.* 913  
*Fluids* **92**, 215–225 (2022). 914
- Villafruela, J. M., Olmedo, I., De Adana, M. R., Méndez, C., and Nielsen, P. V., 915  
"CFD analysis of the human exhalation flow using different boundary condi- 916  
tions and ventilation strategies," *Build. Environ.* **62**, 191–200 (2013). 917
- Wang, P., Zhang, Y., and Guo, Z., "Numerical study of three-dimensional natural 918  
convection in a cubical cavity at high Rayleigh numbers," *Int. J. Heat Mass* 919  
*Transfer* **113**, 217–228 (2017). 920
- Weller, H., Tabor, G., Jasak, H., and Fureby, C., "A tensorial approach to compu- 921  
tational continuum mechanics using object-oriented techniques," *Comput.* 922  
*Phys.* **12**, 620 (1998). 923
- World Health Organization, Regional Office for Europe, *WHO Guidelines for* 924  
*Indoor Air Quality: Selected Pollutants* (World Health Organization, Regional 925  
Office for Europe, 2010). 926
- Xu, G. and Wang, J., "CFD modeling of particle dispersion and deposition cou- 927  
pled with particle dynamical models in a ventilated room," *Atmos. Environ.* 928  
**166**, 300–314 (2017). 929
- Yang, R., Ng, C. S., Chong, K. L., Verzicco, R., and Lohse, D., "Do increased flow 930  
rates in displacement ventilation always lead to better results?," *J. Fluid Mech.* 931  
**932**, A3 (2022). 932
- Yerragolam, G. S., Howland, C. J., Yang, R., Stevens, R. J., Verzicco, R., and 933  
Lohse, D., "Effect of airflow rate on CO<sub>2</sub> concentration in downflow indoor 934  
ventilation," *Indoor Environ.* **1**(2), 100012 (2024). 935